

See discussions, stats, and author profiles for this publication at: <https://www.researchgate.net/publication/51104064>

# Understanding and Controlling Organic-Inorganic Interfaces in Mesostructured Hybrid Photovoltaic Materials

ARTICLE in JOURNAL OF THE AMERICAN CHEMICAL SOCIETY · JUNE 2011

Impact Factor: 12.11 · DOI: 10.1021/ja200054z · Source: PubMed

---

CITATIONS

32

---

READS

44

8 AUTHORS, INCLUDING:



**Aditya Rawal**

University of New South Wales

33 PUBLICATIONS 452 CITATIONS

SEE PROFILE



**Tamar Segal-Peretz**

Argonne National Laboratory

16 PUBLICATIONS 105 CITATIONS

SEE PROFILE



**Dan Huppert**

Tel Aviv University

120 PUBLICATIONS 2,867 CITATIONS

SEE PROFILE


# Understanding and Controlling Organic–Inorganic Interfaces in Mesostructured Hybrid Photovoltaic Materials

S. Neyshtadt,<sup>†</sup> J. P. Jahnke,<sup>‡</sup> R. J. Messinger,<sup>‡</sup> A. Rawal,<sup>‡</sup> T. Segal Peretz,<sup>†</sup> D. Huppert,<sup>§</sup>  
B. F. Chmelka,<sup>\*,‡</sup> and G. L. Frey<sup>\*,†</sup>

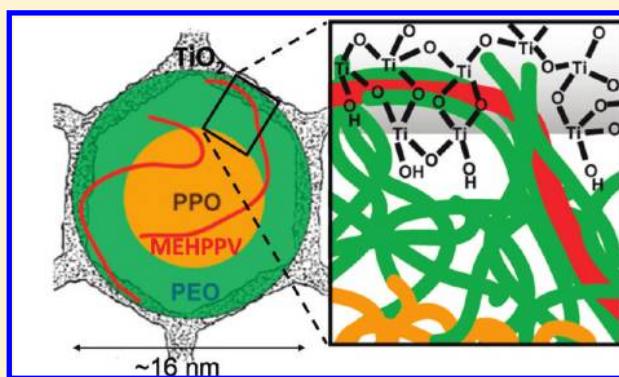
<sup>†</sup>Department of Materials Engineering, Technion - Israel Institute of Technology, Haifa 32000, Israel

<sup>‡</sup>Department of Chemical Engineering, University of California, Santa Barbara, California 93106, United States

<sup>§</sup>Raymond and Beverly Sackler Faculty of Exact Sciences, School of Chemistry, Tel Aviv University, Tel Aviv 69978, Israel

 Supporting Information

**ABSTRACT:** The chemical compositions and structures of organic–inorganic interfaces in mesostructurally ordered conjugated polymer–titania nanocomposites are shown to have a predominant influence on their photovoltaic properties. Such interfaces can be controlled by using surfactant structure-directing agents (SDAs) with different architectures and molecular weights to promote contact between the highly hydrophobic electron-donating conjugated polymer species and hydrophilic electron-accepting titania frameworks. A combination of small-angle X-ray scattering (SAXS), scanning and transmission electron microscopy (SEM, TEM), and solid-state NMR spectroscopy yields insights on the compositions, structures, and distributions of inorganic and organic species within the materials over multiple length scales. Two-dimensional NMR analyses establish the molecular-level interactions between the different SDA blocks, the conjugated polymer, and the titania framework, which are correlated with steady-state and time-resolved photoluminescence measurements of the photoexcitation dynamics of the conjugated polymer and macroscopic photocurrent generation in photovoltaic devices. Molecular understanding of the compositions and chemical interactions at organic–inorganic interfaces are shown to enable the design, synthesis, and control of the photovoltaic properties of hybrid functional materials.



## ■ INTRODUCTION

Nonionic amphiphilic surfactants are known to direct the formation of ordered inorganic mesostructured materials,<sup>1–3</sup> including self-assembly from volatile solutions as solvents evaporate.<sup>4–8</sup> Sol–gel chemistry allows a wide range of densely cross-linked mesostructured oxide frameworks to be prepared from soluble network-forming oxide precursors,<sup>5,9,10</sup> which coassemble with hydrophilic surfactant moieties as solvent species evaporate.<sup>4,11,12</sup> The characteristic periodicities and dimensions of the resulting inorganic–organic hybrid materials are determined principally by the chemical compositions and molecular weights of the surfactant structure-directing agents (SDAs) used. Uniform characteristic length scales can be produced from several to tens of nanometers, with typical length scales for commonly used SDAs, such as the Brij or Pluronic-type surfactants, being between 5 and 20 nm.<sup>2,3</sup>

Recently, there have been extensive efforts to exploit the high internal surface areas and nanoscale dimensions of inorganic–organic nanocomposites to overcome several current limitations of hybrid photovoltaic (PV) materials. These include the degree to which excitons dissociate into free carriers, which is generally considered to severely limit the photovoltaic performance of

devices based on light-absorbing organic molecules, including conjugated polymers.<sup>13</sup> A common means of enhancing such dissociation is to blend the donor and acceptor materials, both organic or hybrid organic–inorganic components, to form a heterojunction material.<sup>14</sup> However, the small exciton diffusion lengths of organic chromophore assemblies and conjugated polymers, about 5–10 nm,<sup>15–17</sup> underscore the importance of high-surface-area interpenetrating donor–acceptor networks with nanosize domains, such as those provided by SDA-directed hybrid materials. Device architectures also require that each phase maintains continuity through the active layer to provide continuous pathways for carrier transport to the respective electrodes.<sup>14,18–20</sup> Furthermore, the donor and acceptor must have a suitable energy-band alignment to allow exciton dissociation and to provide a high overall electrochemical potential, which constrain the types and ranges of suitable chemical compositions and interactions at the donor–acceptor interfaces.

Among the numerous possible donor and acceptor pairs, poly phenylenevinylene (PPV)-type conjugated polymers with titanium

Received: January 16, 2011

Published: May 06, 2011

dioxide ( $\text{TiO}_2$ ) have been widely explored in the context of photovoltaic devices.<sup>21,22</sup> These species are attractive in combination, due to the strong absorption by the conjugated polymer in the visible range of the electromagnetic spectrum, their interfacial energy band offset which favors the transfer of photoexcited electrons from the PPV moieties to  $\text{TiO}_2$ , and the mechanical robustness endowed by continuous inorganic  $\text{TiO}_2$  networks.<sup>23</sup> However, poor miscibility between hydrophilic  $\text{TiO}_2$  sol–gel precursors and hydrophobic conjugated polymers often leads to macroscale phase separation, which can result in low extents of mixing between the two materials and correspondingly low interfacial contact that limits exciton dissociation efficiency.<sup>24,25</sup>

The incompatibility between hydrophilic titanium dioxide and hydrophobic conjugated polymers can be circumvented by using SDAs, such as amphiphilic block copolymers or low-molecular-weight surfactants, which self-assemble into structures where hydrophilic and hydrophobic domains are in nanoscale proximities to each other. Recently, we have shown that SDAs can be used to improve interfacial contact and exciton dissociation between a metal oxide and conjugated polymer by directing the deposition of mesostructured conjugated polymer-containing metal oxide films with interpenetrating organic–inorganic networks.<sup>26–28</sup> These films are prepared by coassembling metal oxide precursor, highly hydrophobic conjugated polymer, and SDA species from tetrahydrofuran (THF) solutions.<sup>26</sup> Meso-scale organization of the conjugated polymer species with the hydrolyzing metal oxide precursor and subsequently cross-linked framework is directed through self-assembly of the SDA. The type of mesostructural ordering that results, for example, lamellar, hexagonal, or cubic, depends on the solution composition and processing conditions. In these experiments, SDA concentrations and relative humidities were chosen to induce the formation of mesostructured films with through-film interpenetrating (e.g., cubic) organic–inorganic networks. Such mesostructured metal oxide films are well suited for the integration of conjugated polymer guest species as the active component in light-emitting diodes and photovoltaic devices.<sup>26,28,29</sup>

Until now, SDAs have generally been used to improve donor–acceptor mixing<sup>30,31</sup> and/or to direct the structure into through-film interpenetrating donor–acceptor networks necessary for opto-electronic applications.<sup>26,32–34</sup> However, limited molecular understanding or control of the inhomogeneous interface structures and compositions have been demonstrated, despite their importance to exciton dissociation and to overall device performance. It is expected that during self-assembly of the SDA, the highly hydrophobic conjugated polymer species associate with the relatively hydrophobic SDA aggregates. Furthermore, the extent to which the conjugated polymer guests interact with the hydrophilic titania framework is hypothesized to depend on the respective interfacial contacts of the different SDA blocks with the titania framework, which are influenced by the molecular weight and chemical composition of the SDA species. These affect organic–inorganic interactions, interfacial compositions, and proximities between dissimilar species, which are crucial for the electronic, photophysical, or chemical processes that directly account for photovoltaic device performance.

Here, we show for the first time that molecular understanding of SDA interactions with the cross-linking metal oxide species and the conjugated polymer can be used to direct the structure and composition of the organic–inorganic interface and thereby mediate resulting photovoltaic properties. More specifically, judicious selection of SDA molecular weight and chemical composition

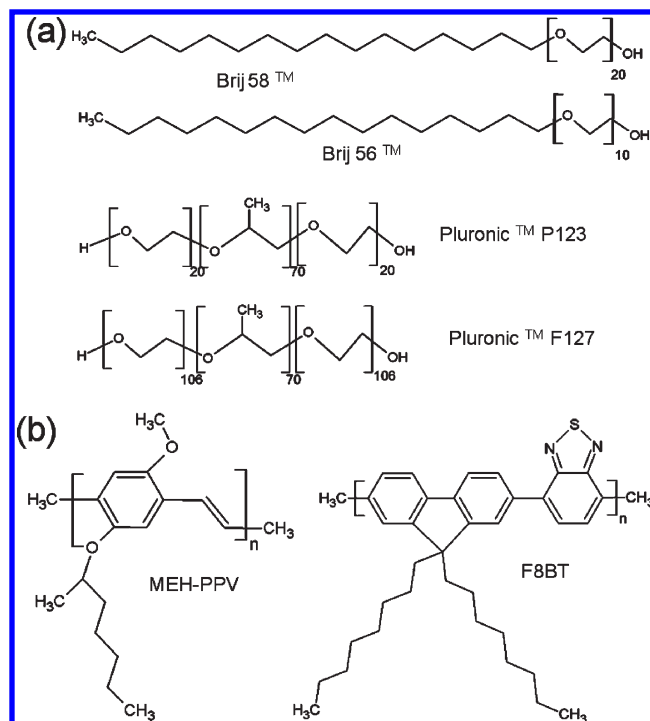


**Figure 1.** (a) Chemical formulas of the four structure-directing agents (SDAs) used in this study: alkyl-ethyleneoxide  $\text{C}_n\text{H}_{2n+1}(\text{EO})_m$  surfactants Brij58 ( $n = 8, m = 20$ ) and Brij56 ( $n = 8, m = 10$ ); and polyethyleneoxide-polypropyleneoxide-polyethyleneoxide  $\text{EO}_x\text{PO}_y\text{EO}_x$  triblock copolymers Pluronic P123 ( $x = 20, y = 70$ ) and Pluronic F127 ( $x = 106, y = 70$ ). (b) Chemical formulas of the conjugated polymers incorporated into the mesostructured SDA-titania composites examined: MEHPPV poly[2-methoxy-5-(2'-ethyl-hexyloxy)-1,4-phenylenevinylene] and F8BT poly[9,9'-dioctylfluorene-co-benzothiadiazole].

promotes dispersal of the conjugated polymer species within different SDA domains, which influences and can be used to control the distribution of the conjugated species with respect to the titania framework. Such distributions are manifested directly by solid-state NMR and energy-filtered TEM, and indirectly by photoluminescence properties or the macroscopic performances of photovoltaic devices comprised of interpenetrating conjugated polymer-titania mesostructured films. Photocurrents are generated by electron transfer from photoexcited conjugated polymers (donor) to the titania framework (acceptor) across their mutual interface. Accordingly, mesostructured films containing SDAs that promote close proximities and strong interactions between the conjugated polymer species and the titania show more efficient photocurrent generation and improved photovoltaic properties, compared to films synthesized with SDAs that result in weaker interactions between the titania and conjugated polymer species. Establishing the effects of interfacial compositions and structures on material functionality is important generally for achieving desirable properties in heterostructured materials.

## EXPERIMENTAL SECTION

**Materials.** Titanium tetraethoxide (TEOT, Aldrich Germany), concentrated 12 M hydrochloric acid (HCl) in deionized water (Carlo Erba, Italy), and tetrahydrofuran (THF AR, BioLab, Israel) were used as-received. Two structure-directing surfactant triblock poly(ethyleneoxide)-*b*-poly(propyleneoxide)-*b*-poly(ethyleneoxide)

**Table 1. Molar Ratios of Reagents in the Precursor Solutions Used to Prepare the Mesostructured Titania-SDA-MEHPPV Hybrid Photovoltaic Materials in This Study, along with the Calculated Weight Percents of MEHPPV in the Product Films**

SDA	TEOT	HCl	H <sub>2</sub> O	SDA	THF	MEHPPV
F127	1	0.9	3	0.004	12	0.49 wt %
P123	1	0.9	3	0.009	12	0.47 wt %
Brij56	1	0.9	3	0.14	12	0.33 wt %
Brij58	1	0.9	3	0.08	12	0.36 wt %

copolymers were obtained as gifts from BASF, USA, and used as-received: EO<sub>20</sub>PO<sub>70</sub>EO<sub>20</sub> (Pluronic P123,  $M_n = 5750$  g/mol), and EO<sub>106</sub>PO<sub>70</sub>EO<sub>106</sub> (Pluronic F127,  $M_n = 12\,600$  g/mol), where “EO<sub>*x*</sub>” and “PO<sub>*y*</sub>” represent the lengths of the ethyleneoxide and propyleneoxide blocks, respectively. The Pluronic triblock copolymers P123 and F127 are composed of relatively hydrophobic center propyleneoxide blocks (PO) of identical mean lengths (70 PO monomer units), and two hydrophilic ethyleneoxide blocks (EO) on each end that are substantially shorter (20 EO units each) for P123 than for F127 (106 EO units each). Two low-molecular-weight  $C_nH_{2n+1}(EO)_m$  surfactants were purchased from Aldrich: Brij56 ( $n = 16, m = 10, M_w = 683$  g/mol) and Brij58 ( $n = 16, m = 20, M_w = 1125$  g/mol). Compared to the Pluronic triblock copolymers, the Brij surfactants are diblocks composed of short hydrophilic ethyleneoxide segments (10 and 20 EO monomer units for the Brij56 and Brij58, respectively) and C<sub>16</sub>H<sub>33</sub> alkyl chains that are significantly more hydrophobic than the propyleneoxide blocks of the Pluronics. Two types of conjugated polymers were purchased from ADS, Canada, and used as-received: poly[2-methoxy-5-(2'-ethyl-hexyloxy)-1,4-phenylenevinylene] (MEHPPV,  $M_w = 480\,000$  g/mol) and poly[9,9'-dioctyl-fluorene-co-benzothiadiazole] (F8BT,  $M_w = 22\,000$  g/mol). MEHPPV is commonly used in photovoltaic devices with titania as a donor/acceptor pair and F8BT is useful as a TEM marker, due to its sulfur atoms that provide distinct signals in energy-filtered TEM images. Both molecules are highly hydrophobic and are expected to have similar interactions and locations within the titania-SDA mesostructured films. The molecular structures of the SDAs and conjugated polymers used in this study are shown in Figure 1a,b, respectively. An aqueous dispersion of poly(3,4-ethylenedioxythiophene)-poly(styrenesulfonate), (PEDOT:PSS), acquired from BAYTRON F E, was used as a conductive layer in the photovoltaic devices. Perdeuterated solvents: d<sub>8</sub>-THF (D, 99.5%), D<sub>2</sub>O (D, 99.9%), and DCl (D, 99.5%, 35 wt % in D<sub>2</sub>O), were purchased from Cambridge Isotope Laboratories (CIL) Inc. and used as-received.

**Syntheses.** In a typical synthesis, TEOT was hydrolyzed by addition of 0.35 mL of 12 M HCl to 1 mL of liquid TEOT, after which the mixture was vigorously stirred for 10 min or until the solution was clear. Upon mixing, a slight color change of the solution was observed from colorless to light yellow. Separately, a THF solution of the structure-directing surfactant species was prepared, according to the molar compositions shown in Table 1. After stirring, the surfactant solution was added to the TEOT solution, and the mixture was stirred for two hours.

To incorporate MEHPPV into the mesostructured titania-SDA films, 0.75 mg of MEHPPV dissolved in 1.5 mL of THF was added to the TEOT/surfactant solution and the mixture stirred for 2–3 min before film deposition. Thin films were prepared by dip-coating on glass, silicon, polyimide, or PEDOT:PSS coated indium–tin-oxide (ITO) substrates and were subsequently characterized by optical, HR-SEM, SAXS, and current–voltage measurements. The dip-coating was performed at a speed of 2 mm/s in an environmentally controlled chamber with a relative humidity of 70–80% to compensate for the water deficiency of the solution and to promote formation of cubic mesophases.<sup>35,36</sup>

The loadings of conjugated polymer species in the mesostructured titania films were estimated, based on the relative amounts of the

components in the precursor solutions, to be approximately 0.49, 0.47, 0.36, and 0.33 wt % for films prepared with Pluronic F127, Pluronic P123, Brij58, and Brij56, respectively. Precise determination of the conjugated polymer loading is challenging due to the low concentration of the conjugated polymer and the small total masses of the product films.<sup>28</sup> The synthesis compositions from which the different mesostructured titania-SDA-MEHPPV films were prepared are summarized in Table 1.<sup>37</sup>

To improve spectral resolution of <sup>1</sup>H moieties, the samples for NMR characterization were synthesized from precursor solutions by using the perdeuterated solvents DCl, D<sub>2</sub>O, and d<sub>8</sub>-THF, following the compositions listed in Table 1. Higher weight percents of MEHPPV were used in the NMR samples (2.6, 2, and 6 wt % for materials synthesized with P123, Brij56 and F127, respectively) to increase the signal intensities in the two-dimensional (2D) NMR measurements without affecting the overall mesostructural ordering in the product materials. Approximately 250-μm-thick films were drop-cast on Teflon substrates and left in high relative humidity (ca. 90%) to reduce the rate of drying until complete after approximately 3 weeks.

**Characterization.** Small-angle X-ray scattering (SAXS) patterns were acquired on films deposited onto polyimide substrates that were measured using a Bruker Nanostar diffractometer (KFF CU 2 K-90) with Cu K<sub>α</sub> radiation ( $\lambda = 1.542$  Å, voltage 40 keV, current 20 mA) in “glancing incidence” geometry, with an incident angle of 2°. The patterns were recorded by a 2D position-sensitive wire detector situated 64.3 cm behind the sample.

High-resolution (HR) transmission electron microscopy (TEM) measurements were conducted using a Philips CM120 microscope operating at a voltage of 120 keV or a FEI Tecnai G2 T20 S-Twin microscope operating at 200 keV. High-resolution scanning electron microscopy (SEM) images were acquired using a LEO Gemini 982 field emission gun with an accelerating voltage of 1–4 keV. Generally, the films were calcined at 450 °C prior to HRSEM imaging. Energy-filtered (EF) TEM measurements were performed using a FEI Titan 80–300 KeV S/TEM operating at 200 keV with filters set to the sulfur L<sub>2,3</sub> edge (165 eV) or to the titanium L<sub>2,3</sub> edge (460 eV). Samples for EF-TEM examination were thinned using a Focused Ion Beam integrated in the Strata 400 STEM DualBeam system of a Field-Emission Scanning Electron Microscope (FE-SEM).

Photoluminescence measurements were conducted using a Varian Cary Eclipse fluorescence spectrometer. Both MEHPPV and F8BT were excited at 420 nm through a 400–500 nm band-pass filter. Temporal decay measurements were performed using a TCSPC detection system, based on a Hamamatsu 3809U photomultiplier and an Edinburgh Instruments TCC 900 computer module. The sample was excited using the second harmonic of a mode locked Ti:sapphire laser.<sup>38</sup> The overall instrumental response time was approximately 42 ps (full-width-at-half-maximum, fwhm). The excitation wavelength was 430 nm for all time-resolved measurements, and the detection wavelength was 575 and 535 nm for MEHPPV and F8BT, respectively.

Solid-state 2D <sup>13</sup>C{<sup>1</sup>H} heteronuclear and <sup>1</sup>H{<sup>1</sup>H} homonuclear correlation NMR experiments were conducted at 11.7 T using a Bruker AVANCE II spectrometer operating at frequencies of 500.24 MHz for <sup>1</sup>H and 125.79 MHz for <sup>13</sup>C. The experiments were performed under magic-angle-spinning (MAS) conditions using either a 4-mm double-resonance variable-temperature Bruker MAS probehead or a 1.3-mm double-resonance Bruker MAS probehead for fast MAS speeds. Experiments were conducted at room temperature or at lower temperature (273 K) to reduce the molecular mobilities of the surfactant moieties and thereby enhance the efficiency of <sup>13</sup>C cross-polarization and <sup>1</sup>H spin diffusion. <sup>1</sup>H T<sub>2</sub> relaxation times were measured by using a series of rotor-synchronized Hahn-echo experiments. Cross-polarization was used to transfer magnetization from <sup>1</sup>H to <sup>13</sup>C nuclei by adiabatic passage through the Hartmann–Hahn condition.<sup>39</sup> Heteronuclear <sup>1</sup>H decoupling was applied during signal acquisition at a <sup>1</sup>H nutation frequency of 100 kHz by



using the pulse sequence SPINAL-64.<sup>40</sup> Quadrature detection in the indirect  $^1\text{H}$  dimension was achieved by using time-proportional-phase-incrementation (TPPI).<sup>41</sup> The 2D spectra were acquired by using a recycle delay of 1 s, and 1024 transients were signal-averaged for each of 128  $t_1$  increments. The 2D  $^{13}\text{C}\{^1\text{H}\}$  HETCOR spectra were generally acquired under MAS conditions of 12.5 kHz with a 2 ms CP contact time and with high power  $^1\text{H}$ – $^1\text{H}$  homonuclear decoupling using the eDUMBO-1<sub>22</sub> sequence applied during the proton spin evolution time with a phase-modulated r.f. pulse of constant amplitude (100 kHz).<sup>42</sup> In the indirect (proton) dimension, a scaling factor of  $\lambda = 0.623$ – $0.638$  was calibrated from separate 2D  $^1\text{H}\{^1\text{H}\}$  spin diffusion NMR experiments. When narrow  $^1\text{H}$  linewidths were present, longer-range and weaker interactions were probed in 2D  $^{13}\text{C}\{^1\text{H}\}$  HETCOR experiments by incorporating a spin-diffusion time of ca. 50 ms, in addition to a 1 ms CP contact time, under MAS conditions of 6 kHz without eDUMBO decoupling (which was unnecessary due to the narrow linewidths). 2D  $^1\text{H}\{^1\text{H}\}$  correlation spectra were acquired under fast MAS conditions of 65 kHz with contact times of 25 ms. Contour levels are shown corresponding to 5, 10, 25, 40, 55, 70, and 85% of the maximum signal intensity.  $^{13}\text{C}$  and  $^1\text{H}$  chemical shifts were referenced to neat tetramethylsilane (TMS, 0 ppm), using tetrakis-methylsilane as an external secondary reference (with  $^{13}\text{C}$  and  $^1\text{H}$  chemical shifts of 3.52 and 0.25 ppm relative to TMS, respectively).<sup>43</sup>

Film thicknesses were measured by using an Alpha-step 200-Tencor profiler and established to be typically 100–150 nm thick for Pluronic-directed films, and 150–200 nm thick for the Brij-directed films. Photovoltaic devices were fabricated by depositing thin films of PEDOT:PSS on  $12 \times 12 \text{ mm}^2$  ITO-coated glass substrates by spin-coating at 1500 rpm, followed by heat treatment for 3 h at 110 °C. The PEDOT:PSS layer protected the ITO from the highly acidic synthesis solution and was found not to alter the device performances, while enhancing reproducibility by reducing ITO corrosion. Following deposition of the respective cubic mesostructured titania-surfactant-MEHPPV films (100–200 nm thick) on the ITO/PEDOT:PSS substrates using the procedure described above, the films were dried in a glovebox, and a thin layer of MEHPPV from a 7 mg/mL xylene solution was spun on top at 1500 rpm in an inert atmosphere. The samples were then heat treated at 90 °C under vacuum for 3 h. Device fabrication was completed by thermal evaporation of a 100-nm-thick gold layer through an eight-pixel shadow mask. The devices were characterized with an Agilent SPA exposed to a 150 W xenon lamp.

## ■ RESULTS AND DISCUSSION

**Coassembly of Mesostructured Titania-SDA-Conjugated Polymer Films.** To incorporate conjugated polymer species within mesostructured metal oxide-SDA composite films during their formation, the hydrophobic conjugated polymer species must coassemble with the SDA surfactant species from solution, together with soluble network-forming inorganic precursor species. The moderate hydrophobicity of THF facilitates solution processing of the dissimilar components, including a wide-range of amphiphilic SDAs and conjugated polymer species, which are highly miscible in THF. As THF evaporates during film processing, the SDA molecules self-assemble, incorporating the highly hydrophobic, high molecular weight, conjugated polymer guest species within the mesostructured inorganic–organic host matrices during their formation.<sup>26</sup> Simultaneously, the hydrolyzed metal oxide (e.g.,  $\text{TiO}_2$ ) precursor species condense, releasing one  $\text{H}_2\text{O}$  molecule for each  $\text{Ti}$ – $\text{O}$ – $\text{Ti}$  bridging moiety formed. The *in situ*-generated water molecules associate preferentially with the hydrophilic blocks of the SDAs, promoting SDA self-organization into liquid-crystal-like mesophases.<sup>27</sup> Concurrent cross-linking of

the metal oxide species results in hybrid inorganic–organic films with high extents of mesostructural order and which incorporate the conjugated polymer functional species within the mesostructured composite matrix.<sup>26</sup>

Although mesostructured metal oxides containing conjugated polymers have shown promise as active layers in light-emitting diodes<sup>26</sup> and photovoltaic devices,<sup>28,44–47</sup> little is known about the distributions of the conjugated polymer species in these complicated heterogeneous materials, or how these distributions may be controlled to influence macroscopic material properties. This is especially true at a molecular level, which has been limited by characterization challenges that have made correlations between synthesis/processing parameters, interfacial compositions and structures, and device performances difficult to establish. To understand the conjugated polymer/surfactant/titania interfaces in mesostructured hybrid photovoltaic materials, films were separately prepared with four related ethyleneoxide-based nonionic SDAs (Pluronic P123 and F127 triblock copolymers, and Brij56 and Brij58 diblock surfactants) with different architectures, compositions, and molecular weights. These SDAs were selected to have different segment lengths and/or hydrophobic–hydrophilic contrast to determine whether and to what extent they influence the compositions and structures of the inorganic–organic interfaces in mesostructured titania materials and their resulting photovoltaic device performances. Under the synthesis conditions described above, these SDAs all direct the formation of similar cubic-like mesostructured titania materials containing conjugated polymer guest species with continuous organic and inorganic networks that facilitate charge transport to the two electrodes during device operation. Such mesostructural ordering is verified by 2D glancing-incidence SAXS, in combination with transmission and scanning electron microscopy.

The 2D glancing-incidence SAXS pattern acquired from a P123-directed titania-MEHPPV film, shown in the inset of Figure 2a, exhibits well-defined spots that are assigned to the (100), (110), and (111) reflections of a rhombohedral  $R3m$  mesostructure with a lattice parameter of  $\sim 14$  nm and a rhombohedral angle of  $\sim 70^\circ$  (Supporting Information, Figure S1 and Equation S1). The presence of a rhombohedral mesostructure, aligned with the (111) planes parallel to the surface, is attributed to distortion of a face-centered cubic ( $Fm3m$ ) mesostructure upon film contraction.<sup>48–51</sup> Cubic-like ordering is confirmed by TEM, a representative image of which is shown in Figure 2a, depicting areas oriented with the [100] and [111] zone axes of the rhombohedral mesostructure (top and bottom, respectively). Cubic-like ordering is also apparent in the HRSEM images in Figure 2b, which exhibit a 6-fold symmetry pattern that is typical of the (111) orientation of a cubic mesostructure. Pluronic F127 directs distorted body-centered cubic ( $Im3m$ )<sup>52</sup> mesostructured films, with a lattice parameter of  $\sim 16$ , from THF precursor solutions, as established by the representative TEM image shown in Figure 2c and the SAXS pattern in its inset (also HRSEM image, Supporting Information, Figure S2).<sup>28,36,52</sup> The distortion of the cubic lattice perpendicular to the surface is likely a result of film contraction during the drying process. The lattice parameters calculated for the P123- and F127-directed cubic mesostructures, along with the dimensions of the bright areas in the TEM images of Figure 2a,c associated with the organic SDA regions, are similar despite the significantly shorter ethyleneoxide blocks of P123 (20 monomer units), compared to those of F127 (ca. 100 monomer units).<sup>53</sup> This suggests that the ethyleneoxide blocks of Pluronic F127 are at least partially occluded within the titania framework,<sup>7,54</sup> as separately established by 2D NMR measurements (see below).

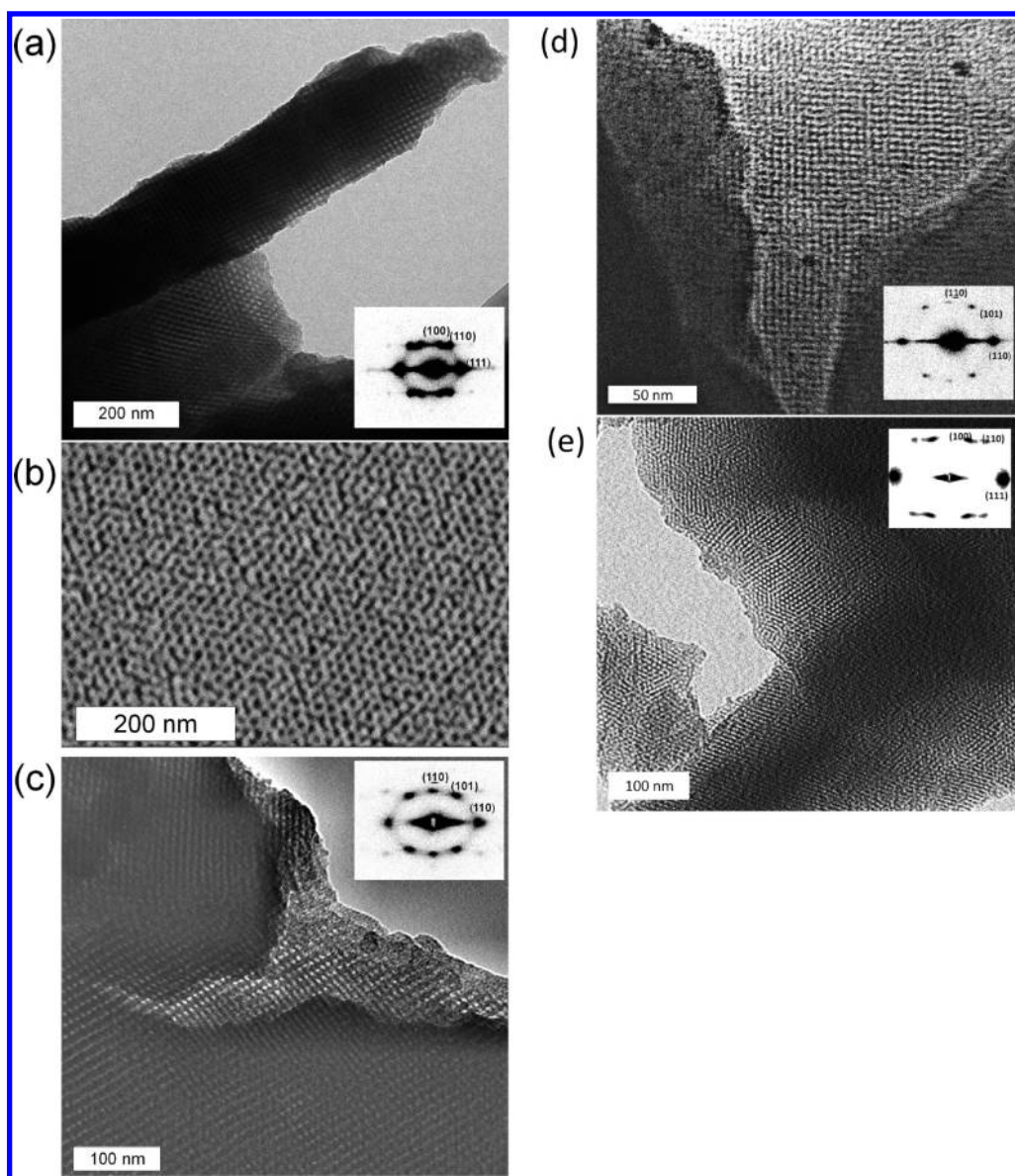


**Figure 2.** (a,c,d,e) Transmission and (b) scanning electron micrographs of cubic mesostructured titania thin films containing ca. 0.4 wt % MEHPPV synthesized using different structure-directing surfactants: (a,b) Pluronic P123, (c) Pluronic F127, (d) Brij58, and (e) Brij56. (Insets) 2D glancing-incidence SAXS patterns, with assigned plane reflections, showing the high degrees of cubic ordering over the 1-mm<sup>2</sup> dimension of the incident X-ray beam in the respective films.

Similar cubic-like mesostructured titania-SDA-MEHPPV films were synthesized from THF precursor solutions using the low-molecular-weight SDAs Brij56 and Brij58, which yield materials with lattice parameters that are significantly smaller than those obtained using the Pluronic triblock copolymer SDAs. The glancing-incidence SAXS pattern in the inset of Figure 2d, acquired for a Brij58-directed titania film, shows the (101), (110), and (110) reflections associated with a distorted cubic *Im3m* mesostructure with an average lattice parameter of about 8 nm, similar to that reported for Brij58-directed titania films deposited from ethanol-based precursor solutions.<sup>36</sup> Such cubic mesostructural order is also observed in the TEM image shown in Figure 2d, which exhibits a grid-like framework with a mean distance of  $\sim 5$  nm between centers, corresponding to a cubic lattice viewed along the (110) direction. The Brij56 SDA directs a mixture of distorted cubic and hexagonal domains, which are

evident in the TEM image and 2D SAXS pattern shown in Figure 2e. The 2D SAXS pattern exhibits intense spots that correspond to the (100), (110), and (111) reflections of a rhombohedral mesostructure (*R3m*) with a lattice parameter of  $\sim 7.5$  nm and a rhombohedral angle of  $70^\circ$ . The rhombohedral phase likely results from contraction normal to the film substrate of a face-centered-cubic (*Fm3m*) mesostructure, as similarly observed for the P123-directed films (Figure 2a). However, the high intensity of the (100) and (111) spots, compared to that of the (110) spot in the Brij56-directed film SAXS pattern (Figure 2e inset), indicates that there is also a weak contribution of reflections from a hexagonal mesophase (calculated lattice parameter  $\sim 8$  nm). The TEM image of a Brij56-directed titania film, Figure 2e, shows 6-fold symmetry that is consistent with either the (111) orientation of a cubic phase or the (001) orientation of the hexagonal phase.



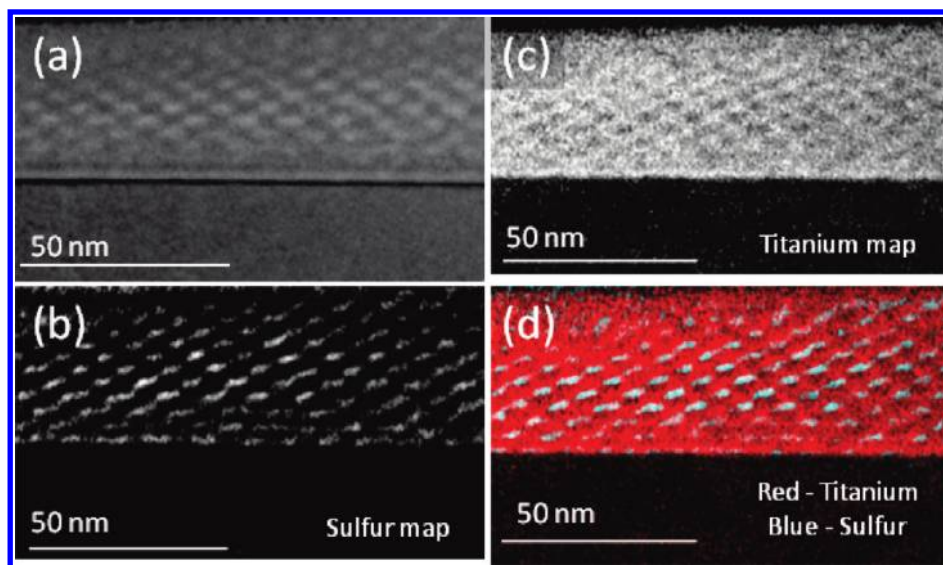


**Figure 3.** High resolution cross-sectional TEM images of a 0.49 wt % F8BT-containing cubic mesostructured titania film synthesized using F127 under (a) bright-field conditions, and corresponding energy-filtered TEM images of the same sample region using (b) the sulfur  $L_{2,3}$  edge transition (165 eV) or (c) the titanium  $L_{2,3}$  edge (460 eV). Bright intensity in (b) and (c) indicates the locations of sulfur (or titanium)-rich regions in the materials, respectively. For clarity, an overlay of (b) and (c) is presented in (d), where titanium-rich regions appear red and sulfur-rich regions appear blue.

**Mesoscale Partitioning of Conjugated Polymer Species in Hybrid Films.** Although the conditions and different surfactant SDAs used in this study all yield similar cubic-like mesostructured titania, the interfacial contacts between the conjugated polymer guests and the titania host matrices are expected to be influenced by the molecular weights and architectures of the SDAs. Importantly, these interfacial interactions can be used to control processes occurring at the organic–inorganic interfaces, such as exciton dissociation into free carriers in PV devices. Therefore, understanding the interactions among the conjugated polymer guests, the different SDA blocks, and the hydrophilic titania framework is central to establishing and controlling interfacial contacts between specific functionalities.

Indeed, it has been shown that increasing the distance between an electron donor and electron acceptor, such as by placing a spacer between them, reduces the efficiency of the electron transfer.<sup>55–57</sup> For example, when an electron donor such as a thiophene or rhodium dye is separated from titania by a nonconjugated spacer molecule, electron transfer is inhibited, with longer spacer molecules resulting in larger reductions in charge transfer.<sup>58,59</sup> In contrast to systems with well-defined molecular spacers between the electron donors and acceptors, SDA-directed mesostructured titania films containing conjugated polymer guests can have significantly different extents of interfacial proximity. These depend on how the components coassemble during synthesis and film processing, leading to separation distances that vary with and can be decreased by interpenetration of the surfactant into the titania framework.

Interactions among the conjugated polymer guests, the SDA species, and the mesostructured titania host matrix can be established by characterizing the relative distributions of the different molecular species. These can be determined by using a combination of HRTEM and solid-state 2D NMR techniques, which provide complementary insights on where the conjugated polymers are located, correlated with the molecular interactions between the surfactant species and titania framework. More specifically, the elementally distinct signals measured to sub-eV-resolution in

electron energy loss spectroscopy (EELS) are spatially resolved by energy-filtered TEM (EF-TEM), allowing a distribution map of elements within a material to be established. Sulfur atoms, for example, have a strong EELS signature centered at 165 eV, corresponding to the  $L_{2,3}$  loss edge, and hence can be used to map the distribution of sulfur-bearing conjugated polymer guest molecules in the mesostructured titania films. Accordingly, F8BT, a green-emitting conjugated polymer with one sulfur atom per monomer (Figure 1b), was coassembled with F127 (or P123, Supporting Information, Figure S3) and titania precursor species (from a THF solution under identical conditions as used for MEHPPV) to form  $Im3m$  cubic mesostructured titania films containing 0.49 wt % F8BT. TEM images of the same region of this mesostructured film are shown without (Figure 3a) and with (Figure 3b–d) energy filtering. The bright-field TEM image in Figure 3a shows contrast between the highly scattering titania framework (dark features) and weakly scattering organic regions (light features) that reflects the cubic mesostructural ordering of the material. By comparison, the energy-filtered TEM image in Figure 3b of the same area shows intensity contrast between light regions containing sulfur and dark regions that do not. Comparing the two images indicates a clear correlation between the light areas in Figure 3a associated with the hydrophobic SDA regions, and those in Figure 3b corresponding to the sulfur-rich regions. Similar intensity correlations have also been observed for TEM and EF-TEM images of F8BT-containing P123-directed films (Figure S3). Such correlated and complementary bright-field and energy-filtered electron scattering intensities indicate that the highly hydrophobic conjugated polymer species associate with and coassemble with the SDA aggregates, resulting in the F8BT conjugated polymer species being distributed principally within the hydrophobic SDA regions of the cubic mesostructured hybrid film. Similarly, the energy-filtered TEM image in Figure 3c, obtained using the  $L_{2,3}$  edge of titanium, maps the distribution of titania within the same region of the film, exhibiting the cubic mesostructure as expected. Overlaying parts b and c of Figure 3 and their respective sulfur and titania distributions, Figure 3d, clearly shows nanoscale separation of the titania framework

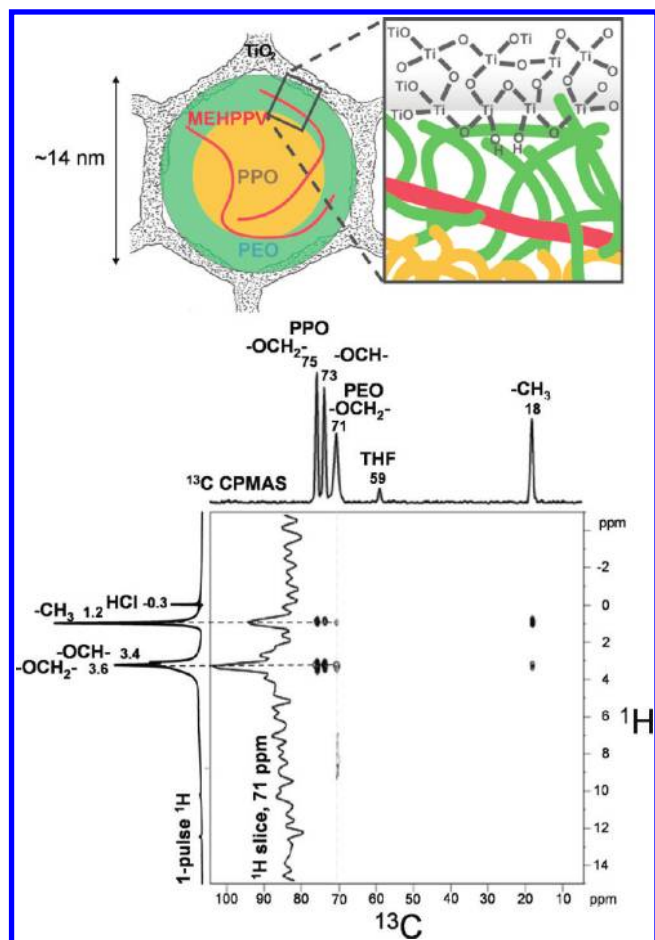


**Figure 4.** Solid-state  $2D\ ^{13}C\{^1H\}$  heteronuclear correlation NMR spectrum acquired at room temperature for mesostructured titania-P123 containing 2.6 wt % MEHPPV under MAS conditions of 6 kHz, with a 1-ms cross-polarization (CP) contact time, and a long (ca. 50 ms)  $^1H$  spin-diffusion time. A 1D single-pulse  $^1H$  MAS and  $^{13}C\{^1H\}$  CP-MAS 1D spectra are shown along the left vertical and top horizontal axes, respectively, of the 2D spectrum. A 1D  $^1H$  slice is shown that corresponds to intensity at 71 ppm in the  $^{13}C$  dimension (vertical dotted line). The schematic diagram shows distributions of titania-P123-conjugated polymer species within a single mesochannel (viewed along the  $(111)$  axis of a cubic structure) that are consistent with the NMR, TEM, and device results: both the EO (green) and PO (yellow) segments of P123 and the MEHPPV guest species (red) are predominantly excluded from the titania framework (gray).

and conjugated polymer species. The sulfur distribution, depicted in Figure 3b, is less well-defined compared to the bright-field TEM image of the same film region (Figure 3a), suggesting partial penetration of the conjugated polymer into the titania framework. As the MEHPPV and F8BT are both highly hydrophobic molecules, they are expected to be distributed similarly within mesostructured titania-SDA films synthesized under otherwise identical conditions.

**Molecular Interfaces in Mesostructured Titania-SDA-Conjugated Polymer Materials.** At a molecular level, the interactions among different species in the mesostructured composites can be established by solid-state 2D NMR techniques that exploit dipole–dipole couplings to correlate the chemical shifts of molecularly proximate moieties. Along with 1D  $^1H$  relaxation-time NMR measurements, these methods yield enhanced spectral or temporal resolution of  $^1H$  and  $^{13}C$  signals associated with

the surfactant, solvent, and/or conjugated polymer species and can establish the relative distributions of the different moieties with respect to each other and the titania framework.  $2D\ ^{13}C\{^1H\}$  HETCOR spectra differentiate among the different  $^1H$  and  $^{13}C$  moieties on the basis of their chemical shifts and provide insights on their molecular mobilities, as manifested by the  $^1H$  linewidths of their resolved signals. For example, Figure 4 shows a  $2D\ ^{13}C\{^1H\}$  heteronuclear correlation (HETCOR) spectrum acquired at room temperature for cubic mesostructured P123-titania containing 2.6 wt % MEHPPV that exhibits well resolved and correlated  $^{13}C$  and  $^1H$  signals associated with the different organic moieties present, specifically the PEO and PPO blocks of the structure-directing P123 triblock copolymer surfactant species. 1D single-pulse  $^1H$  MAS and  $1D\ ^{13}C\{^1H\}$  CP-MAS spectra are shown along the left vertical and top horizontal axes, respectively, to aid interpretation of the 2D HETCOR spectrum. The integrated intensities of the  $1D\ ^{13}C\{^1H\}$  CP-MAS spectrum are influenced by the relative populations and extents of  $^1H$ – $^{13}C$  dipolar coupling associated with the respective  $^{13}C$  moieties, which depend on their intermolecular separation distances ( $\sim 1$  nm) and molecular mobilities ( $> \mu s$  correlation times).<sup>60</sup> The narrow lineshapes observed in both the 1D single-pulse  $^1H$  MAS and  $1D\ ^{13}C\{^1H\}$  CP-MAS spectra yield clearly resolved signals from the various  $^1H$  and  $^{13}C$  moieties, indicating relatively uniform overall environments. This is consistent with the high molecular mobilities of the PEO and PPO segments and their local segregation from the titania framework.

The  $2D\ ^{13}C\{^1H\}$  HETCOR spectrum in Figure 4 of the cubic mesostructured P123-titania-MEHPPV exhibits strong and distinct intensity correlations between  $^1H$  and  $^{13}C$  nuclei associated with the different PEO and PPO blocks of the P123 structure-directing species. The  $^1H$  signal at 1.2 ppm is strongly correlated with the  $^{13}C$  signal at 18 ppm associated with the  $-CH_3$  groups of the PPO blocks, while the  $^1H$  signal at 3.6 ppm exhibits strong correlated intensity with the two  $^{13}C$  signals at 73 and 75 ppm associated with the  $-OCH_2-$  and  $-OCH-$  moieties of the PPO, respectively. Correlated signal intensity is also observed between the  $^1H$  signal at 3.6 ppm and the  $^{13}C$  signal at 71 ppm associated with the  $-OCH_2-$  groups of the PEO blocks. A weaker intensity correlation is also present between the PPO  $-CH_3$   $^1H$  signal at 1.2 ppm and the PEO  $-OCH_2-$   $^{13}C$  signal at 71 ppm, corresponding to relatively weak through-space dipolar interactions among these P123 moieties that are present for the long (50 ms) diffusion time used in the measurement. Weak  $^1H$  intensity is present in the 1D  $^1H$  MAS spectrum in the vicinity of 6–8 ppm (principally from hydrogen-bonded water and  $-OH$  moieties associated with the titania framework),<sup>61</sup> and little, if any,  $^1H$  intensity is observed in this region of the 2D spectrum. This notably includes the 1D  $^1H$  slice taken at 71 ppm in the  $^{13}C$  dimension corresponding to the PEO  $-OCH_2-$  groups, which shows strong and narrow  $^1H$  signals at 1.2 and 3.6 ppm (from the P123 moieties discussed above), but minimal intensity in the region 6–8 ppm. These narrow  $^1H$  signals are furthermore associated with species that exhibit relatively long nuclear spin–spin ( $T_2$ ) relaxation times (ca. 4.1 and 11 ms for the  $-OCH-/-OCH_2-$  and  $-CH_3$  moieties, respectively), which are consistent with high molecular mobilities of the locally segregated P123 blocks. The narrow, uncorrelated  $^1H$  signal at  $-0.3$  ppm is from HCl that arises from exchange among residual protons present in the  $D_2O$  or DCl solvents used in the synthesis.<sup>62</sup> The 2D NMR results thus establish that weak interactions (if any) exist between the P123 species and the titania framework. These analyses are consistent with the energy-filtered TEM images (Figure S3,



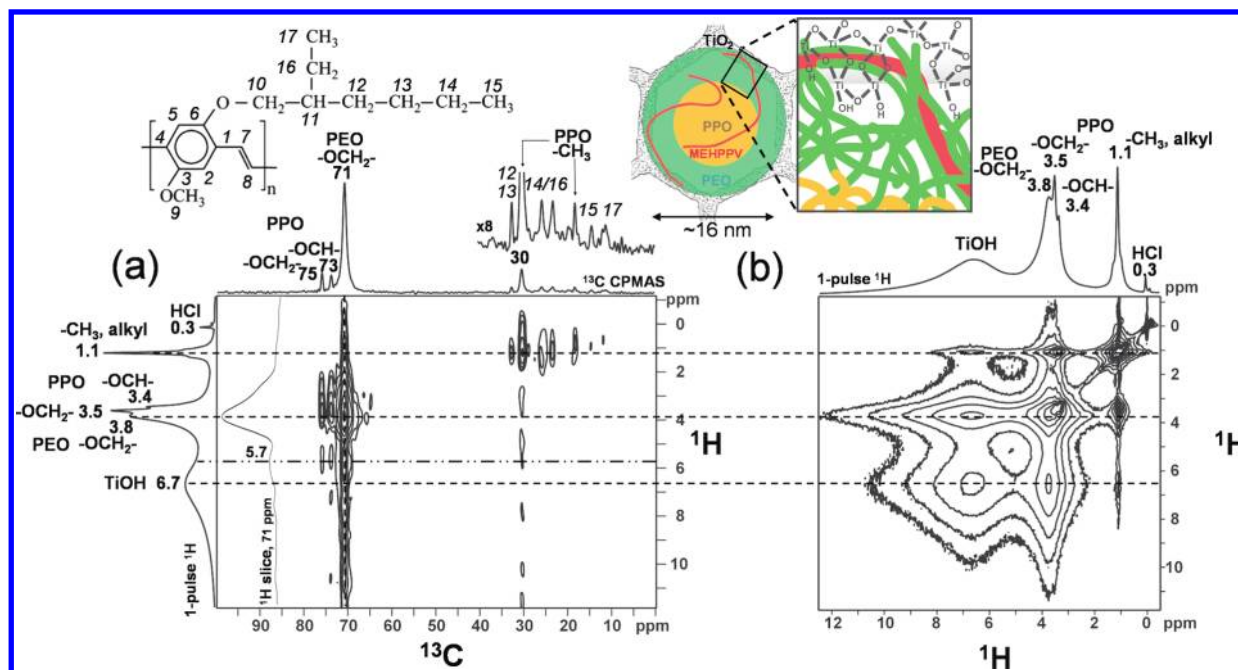


**Figure 5.** Solid-state (a)  $2D\ ^{13}C\{^1H\}$  heteronuclear and (b)  $2D\ ^1H\{^1H\}$  homonuclear correlation NMR spectra acquired at room temperature for mesostructured titania-F127 containing 6 wt % MEHPPV under MAS conditions of 12.5 kHz, with a 2-ms CP contact time. A  $1D\ ^{13}C\{^1H\}$  CP-MAS spectrum is shown along the horizontal axis in (a) with single-pulse  $^1H$  MAS spectra shown on the vertical axis in (a) and the horizontal axis in (b). The  $^1H$  slice in (a) is from the intensity at 71 ppm in the  $^{13}C$  dimension. The schematic diagram shows distributions of titania-F127-conjugated polymer species within a single mesochannel that are consistent with the NMR, TEM, and device results: the long EO (green) segments of F127 interact strongly with and are likely occluded within the titania framework (gray), resulting in close proximity of the MEHPPV guest species (red) to the titania framework.

Supporting Information), which together establish that both the P123 SDA and the conjugated polymer species are incorporated predominantly within the mesochannels of the mesostructured titania-P123 composite in poor contact with the titania matrix.

By comparison, structure-directing species with longer hydrophilic segments, such as Pluronic F127, are expected to exhibit stronger interactions with the mesostructured titania framework. This is supported by the solid-state  $2D\ ^{13}C\{^1H\}$  HETCOR spectrum in Figure 5a acquired for a cubic mesostructured titania-F127 film containing 6 wt % MEHPPV synthesized and characterized under otherwise identical conditions as for the mesostructured titania-P123-MEHPPV films discussed above. An important difference between the materials prepared with the different SDAs is the longer ethyleneoxide blocks associated with F127 (ca. 100 EO groups each), compared to P123 (ca. 20 EO units each). The  $2D\ ^{13}C\{^1H\}$  HETCOR spectrum (Figure 5a) was acquired at room temperature under MAS conditions of 12.5 kHz and using eDUMBO  $^1H$  decoupling to reduce  $^1H$ – $^1H$  dipolar couplings during the evolution period and thereby ensure that the broader  $^1H$  signals associated with mesostructured titania-F127 composite are due to a heterogeneous distribution of local chemical environments. As for the mesostructured titania-P123 material, the  $2D\ ^{13}C\{^1H\}$  spectrum shows well resolved and correlated  $^{13}C$  and  $^1H$  signals associated with the PEO and PPO blocks of the structure-directing F127 triblock copolymer surfactant species, although with significantly broader  $^1H$  signals, especially for the  $-OCH_2-$  PEO moieties. The strongest intensity correlations are observed for the  $-OCH_2-$  groups of the PEO blocks, consistent with their being the major component of the F127 surfactant species. Several  $^1H$  signals are

correlated with the strong PEO  $^{13}C$  signal at 71 ppm; the most intense is the  $^1H$  resonance at 3.8 ppm corresponding to the  $-OCH-$  and  $-OCH_2-$  moieties (as expected), along with a broad signal at ca. 6.7 ppm that is assigned to  $-OH$  or  $H_2O$  moieties associated with the  $TiO_2$  framework.<sup>62</sup> The  $^1H$  signal at 1.1 ppm is also correlated with the  $^{13}C$  signal at 71 ppm, corresponding to PEO  $-OCH_2-$  moieties that are near the  $-CH_3$  groups of the PPO blocks (most likely near PEO–PPO junctures). In addition, this  $^1H$  signal exhibits correlated intensity with alkyl  $^{13}C$  signals between 12 and 33 ppm, which includes the  $^{13}C$  signal at 18 ppm from  $-CH_3$  PPO moieties.

More importantly, the higher concentration of MEHPPV (6 wt %) in the mesostructured titania-F127 films, compared to those synthesized with P123 (2.6 wt %), together with high power  $^1H$  decoupling, allows signals associated with the conjugated polymer species to be resolved and directly observed. Clear 2D intensity correlations in Figure 5a are present between  $^{13}C$  signals at 12, 14, 23, 26, and 33 ppm corresponding to MEHPPV  $^{13}C$  atoms 17, 15, 16, 14, and 12/13 (as labeled) and  $^1H$  signals between 0.5 and 1.4 ppm that are assigned to the alkyl moieties of MEHPPV, based on a separate solid-state  $2D\ ^{13}C\{^1H\}$  HETCOR spectrum acquired for pristine MEHPPV (Supporting Information, Figure S4).<sup>61</sup> Direct molecular evidence for interactions between the MEHPPV and the structure-directing F127 species is manifested by ring-current effects on the NMR signals of both the PEO and PPO moieties of the F127 triblock copolymer. Ring currents arise from the effects of delocalized electrons in  $\pi$ -orbitals in a large magnetic field (e.g.,  $B_0$ ), which induce local fields that affect the isotropic chemical shifts of nearby  $^{13}C$  and  $^1H$  moieties. While such ring-current effects on the  $^{13}C$  signals of alkyleneoxide moieties have been shown to be generally

small ( $<0.5$  ppm), much larger relative displacements (ca. 1 ppm  $^1\text{H}$ ) of their proton signals have been reported.<sup>63</sup> This is consistent with the broadening observed in the  $^1\text{H}$  dimension to lower frequencies (3.5–2.0 ppm  $^1\text{H}$ ) of the  $^{13}\text{C}$  signals at 73 and 75 ppm from the PPO  $-\text{OCH}-$  and  $-\text{OCH}_2-$  groups and at 71 ppm from the PEO  $-\text{OCH}_2-$  moieties. Such broadening is also not observed in otherwise identical samples prepared without MEHPPV (Supporting Information, Figure S5). These interactions most likely occur between MEHPPV and F127 species in the vicinity of the titania framework, where their molecular mobilities are expected to be lower and separation distances close enough that the ring-current effects are not averaged away.<sup>63–65</sup> The narrow and relatively intense alkyl  $^{13}\text{C}$  signal at 30 ppm is consistent with polymer conformation (e.g.,  $\gamma$ -gauche) effects in the hydrophobic MEHPPV side chains<sup>60</sup> and/or their interactions near the hydrophilic titania framework,<sup>66</sup> which may influence local guest environments. This is supported by a 2D  $^{13}\text{C}\{^1\text{H}\}$  HETCOR spectrum (not shown here) acquired under otherwise identical conditions using a longer (8 ms) contact time, in which the  $^{13}\text{C}$  signal at 30 ppm, along with the alkyl  $^{13}\text{C}$  signals associated with the MEHPPV are no longer detected. These observations reflect rapid spin relaxation of these moieties, relative to the other signals associated with the F127 species, including the signal at 18 ppm arising from  $-\text{CH}_3$  PPO groups. Such rapid  $^{13}\text{C}$  spin relaxation of the MEHPPV alkyl moieties is consistent with their lower molecular mobilities near the conjugated MEHPPV backbones and/or framework influences.

Similarly correlated 2D  $^{13}\text{C}\{^1\text{H}\}$  HETCOR signals in Figure 5a also manifest strong molecular interactions between the structure-directing F127 species and the  $\text{TiO}_2$  framework of the cubic mesostructured F127-titania-MEHPPV material. Correlated intensity is observed between the PEO  $^{13}\text{C}$  signal at 71 ppm and  $^1\text{H}$  signal at ca. 6.7 ppm, which reflects strong PEO interactions with hydrogen-bonded  $-\text{TiOH}$  moieties or strongly adsorbed  $\text{H}_2\text{O}$  associated with the titania framework (and possibly proton moieties near the conjugated backbone of MEHPPV).<sup>67</sup> Comparison of the 1D single-pulse  $^1\text{H}$  MAS spectrum with a 1D  $^1\text{H}$  slice extracted from the  $^{13}\text{C}$  dimension at 71 ppm shows that the  $^1\text{H}$  intensity arising from  $-\text{OH}$  moieties of the titania framework is centered ca. 6.7 ppm in the single-pulse  $^1\text{H}$  MAS spectrum, while the  $^1\text{H}$  slice shows that intensity arising from  $-\text{OH}$  groups interacting with  $^{13}\text{C}$  PEO moieties is centered ca. 5.7 ppm. This is consistent with  $-\text{TiOH}$  species interacting via weaker hydrogen-bonds with the F127 moieties and possibly also including contributions from MEHPPV protons. Weaker intensity correlations are also observed for the  $^1\text{H}$  signal at 5.7 ppm with the  $^{13}\text{C}$  moieties associated with the PPO blocks (73 and 75 ppm), consistent with the lower relative lengths of the PPO segments in F127 and reflecting weaker interactions of the PPO moieties with the titania and/or MEHPPV. These  $^1\text{H}$  signals are relatively broad in the  $^1\text{H}$  dimension of the 2D spectrum, particularly those corresponding to the PEO moieties, reflecting their more heterogeneous local environments and lower molecular mobilities that are both attributed to interactions with the titania framework.<sup>7,54</sup> Compared to the P123-titania-MEHPPV material discussed previously, significantly shorter  $^1\text{H}$   $T_2$  relaxation times are measured for all of the F127 moieties (ca. 1.8 and 4.6 ms for the  $-\text{OCH}-$ / $-\text{OCH}_2-$  and  $-\text{CH}_3$  moieties, respectively), which confirm their lower overall mobilities that are consistent with stronger interactions with the titania framework. The correlated 2D  $^{13}\text{C}\{^1\text{H}\}$  HETCOR signal intensities and spin relaxation times measured for the MEHPPV, structure-directing F127, and framework  $-\text{TiOH}$  species provide, direct molecular evidence of their

mutual interactions that manifest the partial inclusion of the conjugated polymer guests within the mesostructured titania host matrix. Such interactions are expected to facilitate charge transfer between the MEHPPV guest species and the  $\text{TiO}_2$  framework.

The 2D  $^1\text{H}\{^1\text{H}\}$  homonuclear correlation NMR spectrum in Figure 5b of mesostructured titania-F127-MEHPPV corroborates the conclusions derived from the 2D  $^{13}\text{C}\{^1\text{H}\}$  HETCOR spectrum discussed above. Several partially resolved  $^1\text{H}$  signals are observed in distinct regions of the spectrum: relatively narrow signal(s) at ca. 1.1 ppm corresponding to the methyl/alkyl moieties of the PPO and MEHPPV species, at ca. 3.4–3.8 ppm corresponding to the  $-\text{OCH}-$  and  $-\text{OCH}_2-$  moieties of the PEO and PPO blocks of F127, and a broad line shape at ca. 5–9 ppm corresponding to hydrogen-bonded  $\text{TiOH}$  and  $\text{H}_2\text{O}$  species within the titania framework and possibly the aromatic moieties of MEHPPV. Extensive correlated  $^1\text{H}$  signal intensity is observed along the spectrum diagonal for all of the species present, indicating that they are spatially near ( $<5$  nm for the 25-ms spin-diffusion time used) and interact with other chemically identical species. This includes  $^1\text{H}$  signals associated with  $\text{TiOH}$  (6.7 ppm),  $-\text{OCH}_2-$  (3.5–3.8 ppm),  $-\text{OCH}-$  (3.4 ppm), and  $-\text{CH}_3$ /alkyl (1.1 ppm), moieties. More importantly, strong off-diagonal  $^1\text{H}$  intensity is observed between the hydrogen-bonded  $-\text{TiOH}$  (6.7 ppm) and the PEO  $-\text{OCH}_2-$  (3.8 ppm) moieties, thereby establishing their mutual proximities and interactions. Weaker off-diagonal  $^1\text{H}$  intensity correlations are additionally present between the titanol  $^1\text{H}$  signals (6.7 ppm) and those corresponding to the methyl/alkyl (1.1 ppm) of the PPO segments (and/or MEHPPV species). Such strong correlated signal intensities in the 2D  $^{13}\text{C}\{^1\text{H}\}$  and  $^1\text{H}\{^1\text{H}\}$  NMR spectra in Figure 5 unambiguously establish that the PEO, and to a lesser extent the PPO, blocks of the structure-directing F127 copolymer species interact strongly with and are most likely occluded within the titania framework. These enhanced interactions between the F127 species and the titania framework, furthermore, promote greater contact between the conjugated polymer guests and the titania matrix, as shown in the schematic diagram accompanying Figure 5.

Compared to the P123 or F127 triblock copolymer structure-directing species discussed above, low-molecular weight surfactants with shorter EO segments and shorter, more hydrophobic alkyl segments are expected to be more compatible with the highly hydrophobic MEHPPV, but yield poorer interfacial contact with the hydrophilic titania matrix. This is confirmed in the 2D  $^{13}\text{C}\{^1\text{H}\}$  HETCOR spectrum in Figure 6 acquired for cubic mesostructured titania synthesized using Brij56 ( $\text{EO}_{10}\text{-C}_{16}\text{H}_{33}$ ) and containing 2 wt % MEHPPV. This spectrum was acquired at 273 K to enhance dipolar couplings between  $^1\text{H}$  and  $^{13}\text{C}$  nuclei associated with the more mobile alkyl chains of the Brij56, whose signals were not observed in a  $^{13}\text{C}\{^1\text{H}\}$  spectrum acquired at 298 K. To aid in the interpretation of the 2D spectrum, two single-pulse  $^1\text{H}$  MAS spectra were acquired at 298 and 273 K under otherwise identical conditions and are shown along the left vertical axis. In the spectrum acquired at 298 K,  $^1\text{H}$  intensity associated with the  $-\text{OCH}_2-$  moieties of Brij56 is observed at 3.4 ppm, with intensity corresponding to the alkyl ( $-\text{CH}_2-$ ,  $-\text{CH}_3$ ) moieties of the Brij56 also clearly resolved at 1.0 and 0.6 ppm, respectively. In the spectrum acquired at 273 K, the reduced mobilities and the correspondingly stronger  $^1\text{H}$ – $^1\text{H}$  dipole–dipole couplings of the Brij56 moieties result in broader, unresolved  $^1\text{H}$  signals for the same moieties with only the signal from  $\text{HCl}$  at  $-0.3$  ppm remaining narrow. Along the top

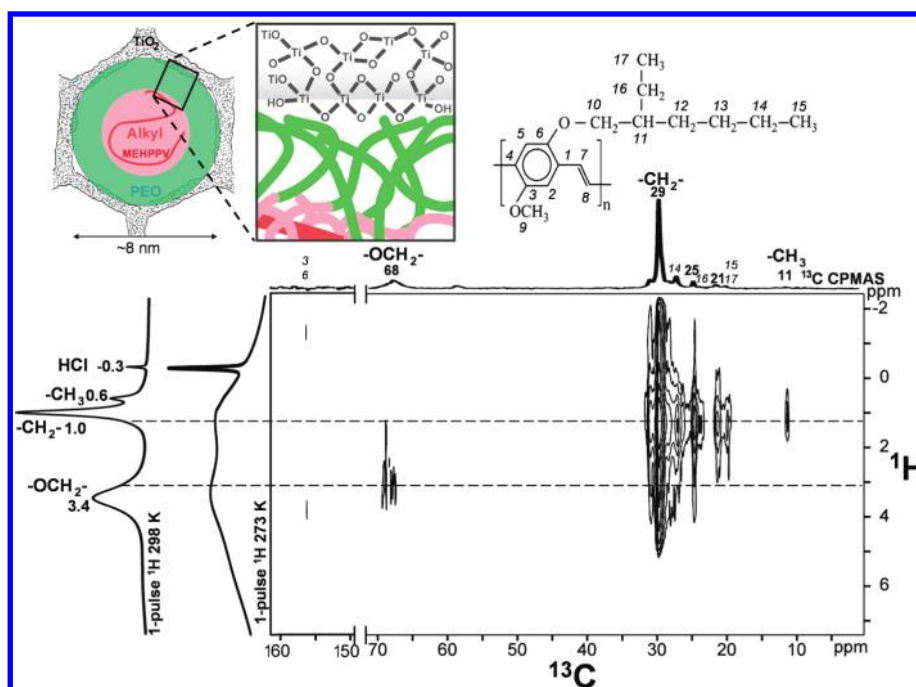


**Figure 6.** Solid-state 2D  $^{13}\text{C}\{^1\text{H}\}$  heteronuclear correlation NMR spectrum acquired at 273 K for mesostructured titania-Brij56 containing 2 wt % MEHPPV under MAS conditions of 12.5 kHz, with a 2-ms CP contact time. A 1D  $^{13}\text{C}\{^1\text{H}\}$  CP-MAS spectrum acquired at 273 K is shown along the top horizontal axis of the 2D spectrum, with 1D single-pulse  $^1\text{H}$  MAS spectra acquired at 298 and 273 K, shown along the left vertical axis. The schematic diagram shows distributions of titania-Brij56-conjugated polymer species within a single mesochannel that are consistent with the NMR, TEM, and device results: the short EO (green) and alkyl (pink) segments of Brij56 and the MEHPPV guest species (red) are predominantly excluded from the titania framework (gray).

horizontal axis, a 1D  $^{13}\text{C}\{^1\text{H}\}$  CPMAS spectrum acquired at 273 K exhibits  $^{13}\text{C}$  signals at 29, and 11 ppm corresponding to the  $-\text{CH}_2-$  and  $-\text{CH}_3$  moieties of the Brij56 alkyl chains, with signals at 25 and 21 ppm corresponding to the  $-\text{CH}_2-$  moieties nearest the ethyleneoxide block and close to the terminal  $-\text{CH}_3$  groups, respectively (Supporting Information, Figure S6). The  $^{13}\text{C}$  signal at 68 ppm corresponds to  $-\text{OCH}_2-$  moieties of the EO segments, with the broad line shape being due to a distribution of local environments that is indicative of low molecular mobility. Additionally, weak  $^{13}\text{C}$  signals at 20, 24, and 27 ppm are resolved from the different alkyl moieties (15/17, 16, and 14, respectively, as labeled in Figure 6) of the MEHPPV guest species. The signals at 20 ppm that correspond to  $^{13}\text{C}$  sites 15 and 17 are shifted by ca. 6–8 ppm from their positions in the spectrum (Figure 5) acquired for the F127-directed composite; this is likely due to the lower temperature and resulting interactions of these moieties with the alkyl chains of the Brij56 surfactant. Although at room temperature the high molecular mobility of the alkyl chains limits their dipolar couplings and corresponding 2D signal intensities, low temperature (273 K)  $^{13}\text{C}$  CPMAS measurements allow all  $^{13}\text{C}$  signals to be detected and resolved, not only for the alkyl and ethyleneoxide segments of the structure-directing Brij56 surfactant, but also the MEHPPV moieties.

The 2D  $^{13}\text{C}\{^1\text{H}\}$  HETCOR experiment allows molecular interactions (or lack thereof) of the Brij56 species with the titania framework and with MEHPPV to be established. In the 2D spectrum (Figure 6) of the cubic mesostructured Brij56-titania-MEHPPV composite, strong correlated intensity is observed between the  $^{13}\text{C}$  signal at 29 ppm and the  $^1\text{H}$  signal at 1.2 ppm, which corresponds to interactions among the  $^1\text{H}$  and  $^{13}\text{C}$  nuclei of the Brij56 alkyl chains. The  $-\text{CH}_2-$   $^{13}\text{C}$  intensity at 29 ppm is also correlated with the  $^1\text{H}$  signal at 3.1 ppm from the  $-\text{OCH}_2-$  groups of the Brij56 surfactant, consistent with the mutual proximities

of these species and the latter being within the corona of the respective hydrophobic channels. Compared to the correlated signals of the alkyl species, the 2D intensities associated with the  $-\text{OCH}_2-$  moieties are weaker due to the larger intermolecular separation distances and relatively rapid  $T_2$  relaxation of the  $-\text{OCH}_2-$   $^1\text{H}$  signal at 273 K. Rapid  $T_2$  relaxation also limits the correlated intensity observed between the  $-\text{OCH}_2-$   $^1\text{H}$  signal at 3.1 ppm and the  $^{13}\text{C}$  signal at 68 ppm from the Brij56  $-\text{OCH}_2-$  moieties. In addition to the  $-\text{CH}_2-$   $^{13}\text{C}$  signal at 29 ppm, the  $^1\text{H}$  signal at 1.2 ppm is correlated with a number of other  $^{13}\text{C}$  signals, including those corresponding to the  $-\text{CH}_3$  moiety at 11 ppm and signals at 25 and 21 ppm that are assigned to the  $-\text{CH}_2-$  moieties nearest the EO segments and close to the terminal  $-\text{CH}_3$  groups of the Brij56, respectively.

Despite the low concentration (2 wt %) of MEHPPV in the Brij56-directed material, intensity correlations associated with the conjugated polymer species are clearly observed in the 2D  $^{13}\text{C}\{^1\text{H}\}$  HETCOR spectrum of Figure 6.  $^{13}\text{C}$  signals at 27, 24, and 20 ppm are also correlated with the alkyl  $^1\text{H}$  intensity at 1.2 ppm and are assigned to the 14, 16, and 15/17  $^{13}\text{C}$  atoms of MEHPPV, respectively. At 273 K, additionally, a very weak signal at 157 ppm in the  $^{13}\text{C}$  dimension is in the region expected for aromatic  $^{13}\text{C}$  atoms (3 and 6) of MEHPPV and is weakly correlated with  $^1\text{H}$  intensity at 3.9 and  $-1.3$  ppm arising from MEHPPV  $-\text{OCH}_3$  (9) and the  $-\text{OCH}_2-$  (10) moieties near these  $^{13}\text{C}$  atoms. In contrast to the F127-directed material, no clear correlated intensity is observed between the  $-\text{OCH}_2-$   $^1\text{H}$  signal (3.1 ppm) of the Brij56 and the  $^{13}\text{C}$  signals of the MEHPPV. In addition, no intensity correlations are observed between  $^1\text{H}$  signals associated with the titania framework (ca. 7 ppm) and  $^{13}\text{C}$  nuclei associated with either the  $-\text{OCH}_2-$  or  $-\text{CH}_2-$  moieties. Correlated signals that could directly indicate interactions between the alkyl groups of the MEHPPV and Brij56 species generally



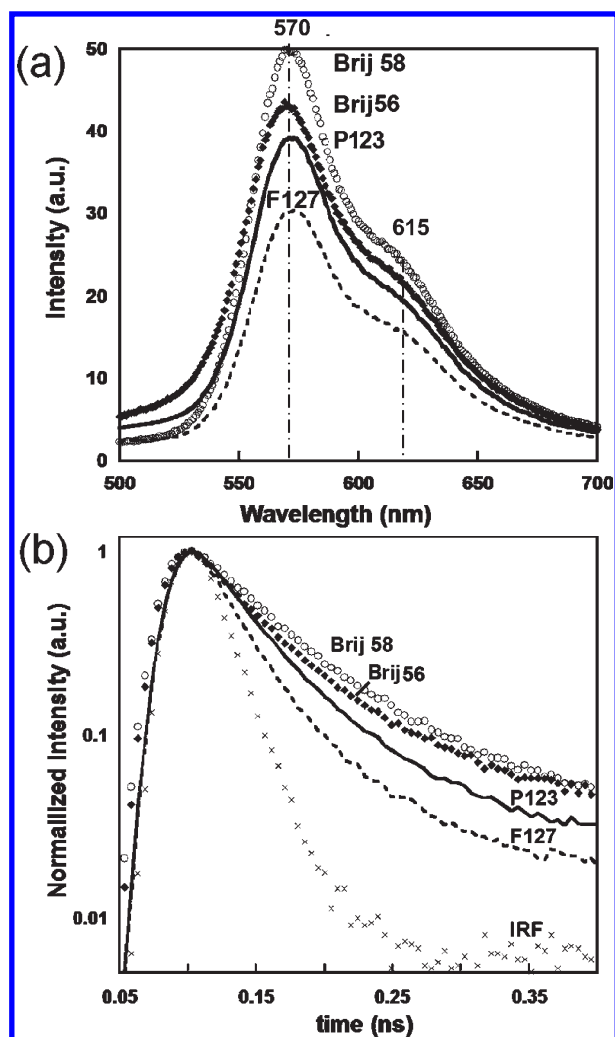


**Figure 7.** (a) Photoluminescence spectra (excitation wavelength 420 nm), and (b) photoluminescence decay curves (acquired at 575 nm) of 100–200 nm-thick mesostructured titania/SDA/MEHPPV thin films, synthesized with different SDAs: F127 (dashed line), P123 (solid line), Brij56 (diamonds), Brij58 (circles). Signals in (a) centered at ca. 570 and 615 nm correspond to the (0,0) and (0,1) vibronic transitions, respectively.<sup>68</sup> The instrument response function (IRF) is denoted by the “x” symbols in (b).

overlap in the  $^1\text{H}$  dimension at 273 and 298 K and cannot be distinguished. Nevertheless,  $^{13}\text{C}$  intensity associated with the Brij56  $-\text{CH}_3$  signal at 11 ppm is broadened asymmetrically to lower frequency in the  $^1\text{H}$  dimension, consistent with MEHPPV-induced ring-current effects previously observed in Figure 5 for the F127-directed material. This suggests that the hydrophobic MEHPPV is preferentially associated with the hydrophobic alkyl segments of the Brij56 surfactant species. Collectively, these observations are consistent with weak interactions between the titania matrix and the Brij56 species, as manifested also by the high mobility of the surfactant species at room temperature, and separately established by  $^1\text{H}$  spin–spin ( $T_2$ ) relaxation time measurements (4.2 ms for  $-\text{OCH}_2-$  and 8.2 ms for  $-\text{CH}_2-$  moieties) at 298 K. Such weak interactions indicate that, in contrast to the Pluronic F127, the short (10 monomer unit) EO segments of the Brij56 surfactant are not embedded within the titania matrix, but rather are locally excluded from the framework, as shown in the accompanying schematic diagram (Figure 6).

Overall, the increased resolution provided by the 2D  $^{13}\text{C}\{^1\text{H}\}$  HETCOR spectra enables detailed understanding of distinctly different molecular interactions and mobilities associated with the different SDA species in mesostructured titania-surfactant films.

**Photovoltaic Properties of Mesostructured Titania-SDA-Conjugated Polymer Materials.** The different extents to which the conjugated polymer species are in contact with the titania framework influence the photovoltaic properties of mesostructured titania materials, according to the distances between the electron donor and acceptor species that affect exciton dissociation. Photoluminescence (PL) experiments may be used to infer relative rates of electron transfer from the conjugated polymer species to the titania matrix, the results of which corroborate the molecular insights gained from the energy-filtered TEM and solid-state NMR measurements. Specifically, increased electron transfer from the conjugated polymer species to the titania framework quenches the photoluminescence of the conjugated polymer species and shortens exciton lifetimes. Accordingly, steady-state and time-resolved PL measurements, which are sensitive to quenching and exciton lifetimes, respectively, provide complementary insights into the interactions between the conjugated polymer and titania in the SDA-directed mesostructured films.

For example, MEHPPV polymer chains incorporated within the SDA-directed cubic-like titania mesostructured films maintain their photoluminescence (PL) properties, as evident from the steady-state PL spectra shown in Figure 7a. The spectra of the mesostructured films share similar spectral features, regardless of the SDA used, and are similar to the PL spectrum of pristine MEHPPV.<sup>28,68</sup> For each of the films, the (0,0) and (0,1) vibronic transitions at ca. 570 and 615 nm, respectively, are observed with similar relative intensities, indicating that the MEHPPV chains in the different films have similar conformations, independent of the SDA used. Furthermore, compared to a solution of MEHPPV in THF, the PL spectra of the mesostructured titania films are red-shifted (about 15–20 nm), demonstrating that energy transfer occurs between polymer chains.<sup>68</sup> However, while the spectral features are similar, their absolute steady-state PL intensities ( $I$ ) are significantly affected by the type of SDA used to synthesize the respective mesostructured films. Higher PL intensity corresponds to less quenching and is associated with weaker interactions between the MEHPPV guest species and the titania framework. As seen in Figure 7a, the absolute intensities exhibit the sequence  $I_{\text{F127}} < I_{\text{P123}} < I_{\text{Brij56}} < I_{\text{Brij58}}$ , consistent with the degree of contact between the MEHPPV species and the titania framework established by the solid-state NMR measurements above. These results suggest that PL quenching is due to fast electron transfer from the photoexcited MEHPPV molecules to the titania framework, as opposed to other slower nonradiative processes, and confirm the importance of interfacial interactions in exciton dissociation.

Fast (<ns) electron transfer processes, such as those between MEHPPV species and mesostructured titania, can be probed quantitatively by PL decay measurements, which measure the persistence of excitons after illumination. Such measurements can thus be used to determine and compare exciton lifetimes in the different mesostructured titania-SDA-MEHPPV films. These notably manifest reductions in PL intensity that can occur due to exciton dissociation through electron transfer to nearby acceptors. Following laser illumination, the PL decay rate is faster when the donor and acceptor are in close proximity and slower when they are farther apart. Figure 7b shows plots of PL intensity as function of time after laser excitation of the similar cubic-like

mesostructured titania-SDA-MEHPPV films analyzed above. Following an initial period (ca. 0.10 ns) during which the measured PL intensity is observed to increase (due to the instrumental response function), comparison of the different plots shows that the exciton decay rate significantly depends on the type of SDA used to synthesize the respective mesostructured films. Films directed by Brij58 have the slowest decay rate (longest lived excited state), followed in sequence by films synthesized with Brij56, P123, and F127, the latter exhibiting the fastest decay (shortest exciton lifetime,  $\tau$ ). The weaker PL quenching in Brij58-directed films compared to that in Brij56-directed films is consistent with the preferential association of the MEHPPV species with the hydrophobic alkyl segments of the Brij surfactants, as indicated by the NMR results (Figure 6). This results in a larger separation distance between the donor and acceptor moieties in the Brij58-directed films, due to the longer hydrophilic segments in Brij58 (ca. 20 EO units, also for P123), compared to Brij56 (ca. 10 EO units). These observations are furthermore consistent with the TEM and X-ray scattering analyses in Figure 2d,e that revealed larger mesochannel dimensions for the Brij58-directed material compared to Brij56, reflecting the larger EO corona associated with the former.

The PL-intensity decay analysis consequently establishes that electron transfer between the MEHPPV guests and the titania framework occurs more readily in the film synthesized with F127 and to increasingly lesser extents in films prepared using P123, Brij56, and Brij58 ( $\tau_{F127} < \tau_{P123} < \tau_{Brij56} < \tau_{Brij58}$ ). Similar time-resolved PL decay measurements of SDA-directed mesostructured titania films containing the green-emitting conjugated polymer F8BT follow this same trend (Supporting Information, Figure S7). These results are consistent with the solid-state 2D NMR analyses (Figures 4–6), which separately established the same sequence for the relative strengths of molecular MEHPPV-SDA-titania interactions in the materials. There is thus excellent correlated agreement among the analyses of PL intensity (Figure 7a),  $I_{F127} < I_{P123} < I_{Brij56} < I_{Brij58}$ , and exciton lifetimes (Figure 7b), with the distributions of the MEHPPV guest species within the mesostructured titania matrices established by the NMR and EF-TEM measurements (Figures 3–6). These results establish the importance and different extents of interfacial contact between the MEHPPV and titania species in the various SDA-directed mesostructured host materials.

Finally, the effects of the organic–inorganic interface compositions and structures in mesostructured titania materials containing conjugated polymer guest species are manifested directly by the macroscopic properties of photovoltaic (PV) devices in which they have been incorporated. Whereas some photovoltaic device properties depend strongly on individual species' properties, such as their energy band levels,<sup>69,70</sup> others are expected to be significantly affected by the degree to which the electron donor and acceptor species interact. This notably includes the short-circuit photocurrent,  $I_{sc}$ , which reflects the net amount of charge carriers flowing through the device at zero bias and which will be strongly influenced by interactions between the donor–acceptor species at their mutual inorganic–organic interface. The  $I_{sc}$  is particularly important, as power generation by a photovoltaic device is a product of only the  $I_{sc}$ , the open-circuit voltage ( $V_{oc}$ , which depends mostly on intrinsic properties of the donor/acceptor components and their contact with the electrodes), and a nonideality or fill factor that varies between 0 and 1.<sup>70</sup> The magnitude of  $I_{sc}$  reflects the light absorption efficiency, the dissociation of the excitons into charge carriers, and the transport of the different carriers across a device to the

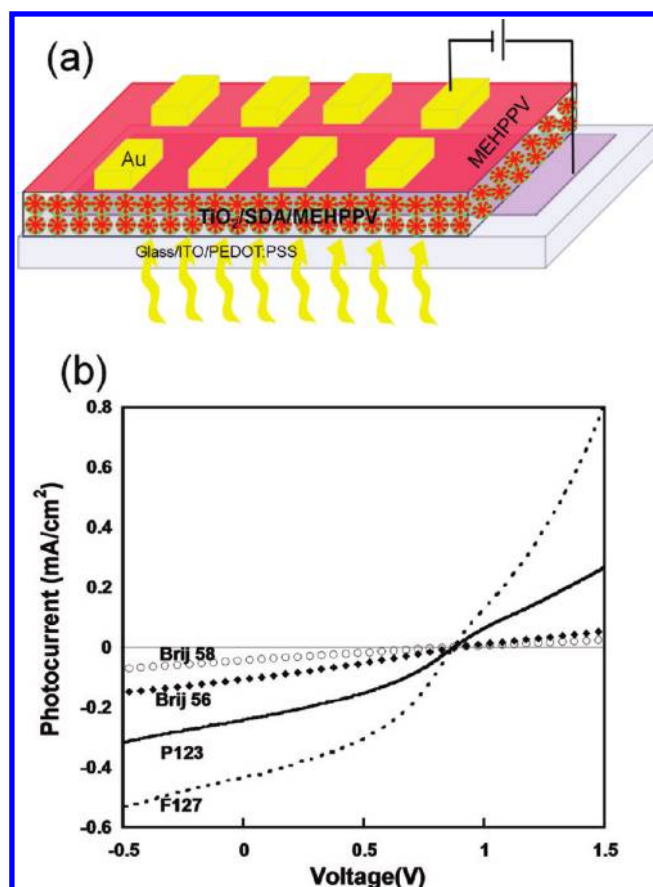


**Figure 8.** (a) Schematic diagram of a photovoltaic device based on a mesostructured titania-SDA-MEHPPV active layer sandwiched between an ITO/PEDOT-PSS anode and a pristine MEHPPV layer covered by a thin Au cathode. (b) Current–voltage curves obtained for photovoltaic devices based on mesostructured titania/SDA-MEHPPV active layers synthesized with different SDAs: F127 (dashed line), P123 (solid line), Brij56 (diamonds), or Brij58 (circles). The zero current line is shown in gray.

electrodes.<sup>71</sup> All of the devices comprised of the mesostructured titania-MEHPPV films prepared in this study, regardless of the type of SDA used, have the same absorbing component (MEHPPV) at similar concentrations, with similar transport pathways (cubic mesostructured titania matrices) and device architectures (e.g., components and film thicknesses). Consequently, the  $I_{sc}$  values are expected to reflect principally the variations in the exciton dissociation efficiency at the titania/MEHPPV interfaces in the different SDA-directed mesostructured films and be correlated with the relative strengths of the molecular interactions and species distributions observed by solid-state NMR, energy-filtered TEM, and steady-state and time-resolved PL.

Cubic-like mesostructured titania films containing MEHPPV and synthesized under identical conditions, except for the use of different F127, P123, Brij58, or Brij56 structure-directing agents, were integrated as the active layer (100–200 nm thick) into photovoltaic devices. Each such device had a configuration comprised of the mesostructured titania-MEHPPV-SDA layer and a separately spin-cast MEHPPV overlayer sandwiched between ITO/PEDOT:PSS and Au electrodes, as schematically shown in Figure 8a.<sup>28</sup> This configuration is similar to the donor–acceptor bulk heterojunction often referred to as the “ideal” nanostructure for

**Table 2. Summary of Photovoltaic Properties and Their Standard Deviations Measured for Devices Containing 100–200 nm-thick Cubic-like Mesostructured SDA-Titania-MEHPPV Films as the Active Layers in Devices with the Configuration Shown in Figure 8a**

cubic mesostructured active layer in PV device	mean $V_{oc}$ (V)	mean $J_{sc}$ (mA/cm <sup>2</sup> )	fill factor (%)	conversion efficiency (%)
F127-titania-MEHPPV	0.86 ± 0.13	0.33 ± 0.10	37 ± 3	0.082 ± 0.038
P123-titania-MEHPPV	0.71 ± 0.24	0.21 ± 0.07	31 ± 3	0.038 ± 0.018
Brij56-titania-MEHPPV	0.79 ± 0.17	0.10 ± 0.03	26 ± 2	0.017 ± 0.003
Brij58-titania-MEHPPV	0.72 ± 0.13	0.04 ± 0.01	25 ± 1	0.006 ± 0.001

photovoltaic applications.<sup>72</sup> Under device operating conditions, light is absorbed by the MEHPPV backbone moieties, producing excitons that can diffuse to interfaces with the nearby (<10 nm) titania framework and dissociate by electron transfer to the titania. The electrons can then be transported within the titania framework to the ITO anode, while the positive charges remain associated with the MEHPPV guest species and are conducted to the separate MEHPPV overlayer and subsequently collected at the gold cathode. Although charge carriers might also be generated at the interface between the mesostructured titania-MEHPPV-SDA film and the MEHPPV overlayer, the contribution of these excitations to the photocurrent is expected to be small (because of the much smaller contact area) and similar for all of the devices examined here, independent of the SDA used.<sup>73</sup>

The macroscopic photovoltaic properties of the devices comprised of different active layers of cubic-like mesostructured titania-MEHPPV-SDA films depend strongly on the chemical composition, architecture, and molecular weight of the SDA used. Current–voltage traces under illumination are shown in Figure 8b and the results summarized in Table 2. Notably, the open-circuit voltages ( $V_{oc}$ ) measured for all of the photovoltaic devices fell within the range 0.71–0.86 V, regardless of the type of SDA used to form the mesostructured titania-MEHPPV active layer. Such similar  $V_{oc}$  values for the devices are consistent with the calculated energy offset  $|E(LUMO)_{\text{acceptor}} - E(HOMO)_{\text{donor}}|$  of the titania and MEHPPV species, confirming that current generation by exciton dissociation at the titania-MEHPPV interfaces occurs in all of the devices.<sup>22</sup> In contrast to the similar  $V_{oc}$  values, the short-circuit current densities ( $J_{sc} = I_{sc}/A$ , where  $A$  is the area of electrode contact) measured for the devices strongly depend on the type of SDA used, with  $J_{sc}$  values decreasing by an order of magnitude according to the sequence  $J_{sc,F127} > J_{sc,P123} > J_{sc,Brij56} > J_{sc,Brij58}$ . Although the  $J_{sc}$  values reported here are significantly lower (by ca. an order of magnitude) than those reported for high performance  $TiO_2$ /polymer photovoltaic devices, mostly due to low polymer loading and low carrier mobility in the conjugated polymer and amorphous  $TiO_x$  regions,<sup>22</sup> they provide important quantitative correlations between macroscopic device properties and the underlying molecular compositions and structures that govern material and device performances. Moreover, the sequence of short-circuit photocurrent values measured for the different SDA-directed materials is in excellent agreement with the same trends previously observed for relative PL quenching efficiency (Figure 7a), exciton lifetimes due to electron transfer from the MEHPPV to titania (Figure 7b), and SDA-mediated interactions between the MEHPPV and titania components established by NMR and EF-TEM (Figures 3–6). These results demonstrate that the technologically important property  $J_{sc}$  which reflects the net amount of photocurrent spontaneously flowing through the device (in the absence of an applied bias), is determined to a significant extent by interfacial interactions among the active and structure-directing species.

## CONCLUSIONS

In summary, structure-directing agents (SDAs) circumvent macrophase separation between highly hydrophobic conjugated polymers and hydrophilic metal oxide donor–acceptor pairs, and additionally allow the compositions, structures, and interactions of active components to be controlled in mesostructured hybrid materials. For cubic mesostructured titania films containing conjugated polymers, molecular-level differences in the interactions among the SDAs, titania frameworks, and conjugated polymer guest species are shown to be correlated with the macroscopic photoluminescence and photovoltaic device properties of otherwise identical materials synthesized with different structure-directing species. More specifically, ethyleneoxide-based SDAs with different lengths of hydrophilic EO segments and different types and lengths of hydrophobic segments, for example, Pluronic P123 and F127 triblock copolymers or low-molecular-weight Brij56 and Brij58 surfactants, result in materials with significantly different interactions among the SDAs, titania, and conjugated polymer guests. Such interactions and distributions of species have been measured at a molecular level by solid-state 2D NMR and energy-filtered TEM measurements, which establish that the distributions of the conjugated polymer guest species in the mesostructured titania-SDA host matrices depend strongly on the chemical compositions, architectures, and molecular weights of the SDAs. Importantly, the interactions of the SDAs with the titania frameworks and the extents to which the hydrophobic conjugated polymer guests interact with the hydrophilic titania framework are enhanced in the presence of SDAs containing long hydrophilic EO segments and moderately hydrophobic PO blocks (e.g., F127), which promote occlusion of these segments and conjugated polymers within the titania matrices. Cubic mesostructured titania-F127-MEHPPV thus exhibits strong SDA-titania-MEHPPV interactions, fast photoluminescence decay rates, and high photocurrent generation. These properties are each independently consistent with enhanced contact between the conjugated polymer guest species and the titania framework, which results in efficient electron transfer at the inorganic–organic interfaces and correspondingly higher photovoltaic device efficiencies. By comparison, mesostructured titania-MEHPPV films synthesized with P123, Brij56, or Brij58 result in weaker SDA-titania-MEHPPV interactions and correspondingly reduced electron transfer efficiency, slower PL decay rates, and diminished photocurrent generation. Such fundamental analyses of the molecular compositions and structures at organic–inorganic interfaces and their correlations to technologically important macroscopic opto-electronic properties are expected to be applicable to hybrid materials in general. The resulting molecular understanding provides opportunities to better control physico-chemical interactions at heterojunction interfaces, thereby yielding selection criteria for the design and syntheses of hybrid functional materials with improved photovoltaic properties.



## ■ ASSOCIATED CONTENT

**S Supporting Information.** Schematic drawing and mathematical description of the rhombohedral  $R3m$  structure; SEM micrograph of a cubic-like F127-titania-MEHPPV film; bright-field and energy-filtered TEM images of a cubic-like P123-titania-F8BT film; solid-state  $2D\ ^{13}C\{^1H\}$  HETCOR NMR spectra of MEHPPV powder and mesostructured titania-F127 acquired at room temperature; PL spectra and decay curves of F127-titania-F8BT and P123-titania-F8BT thin films; and a full list of authors for ref 55. This material is available free of charge via the Internet at <http://pubs.acs.org>.

## ■ AUTHOR INFORMATION

## Corresponding Author

gitti@tx.technion.ac.il

## ■ ACKNOWLEDGMENT

The authors thank Drs. R. Graf, M. Hansen, and D. Dudenko for helpful discussions. The work at the Technion was supported by the Israel Science Foundation under grant No. 943/08, by the Russell Berrie Nanotechnology Institute in the Technion. The work at UCSB was supported in part by the U.S. National Science Foundation under grant nos. CBET-0829182, the USARO through the Institute for Collaborative Biotechnologies under contract no. W911NF-09-D-0001, and by AmberWave, Inc. Drs. Cohen-Hyams and Kauffmann of the Technion Electron Microscopy Center at the Department of Materials Engineering are acknowledged for EF-TEM sample preparation and measurements. The NMR experiments were conducted in the Central Facilities of the UCSB Materials Research Laboratory supported by the MRSEC program of the U.S. NSF under award no. DMR-0520415. J.P.J. acknowledges the U.S. NSF for an IGERT Fellowship under grant NSF-DGE 0801627. R.J.M. acknowledges funding support from the U.S. Department of Energy through the Institute for Multiscale Materials at Los Alamos National Laboratory and a Doctoral Fellowship from the Warren and Katharine Schlinger Foundation. Travel exchange visits between the Technion and UCSB were supported by the EU Marie Curie IRSES FP7 grant no. 230810. B.F.C. was a 2006 Joseph Meyerhoff Visiting Professor at the Weizmann Institute of Science, Rehovot, Israel when this collaborative work was initiated.

## ■ REFERENCES

- (1) Zhao, D. Y.; Huo, Q. S.; Feng, J. L.; Chmelka, B. F.; Stucky, G. D. *J. Am. Chem. Soc.* **1998**, *120*, 6024–6036.
- (2) Zhao, D. Y.; Feng, J. L.; Huo, Q. S.; Melosh, N.; Fredrickson, G. H.; Chmelka, B. F.; Stucky, G. D. *Science* **1998**, *279*, 548–552.
- (3) Bagshaw, S. A.; Prouzet, E.; Pinnavaia, T. J. *Science* **1995**, *269*, 1242–1244.
- (4) Grosso, D.; Cagnol, F.; Soler-Illia, G. J.; de, A. A.; Crepaldi, E. L.; Amenitsch, H.; Brunet-Bruneau, A.; Bourgeois, A.; Sanchez, C. *Adv. Funct. Mater.* **2004**, *14*, 309–322.
- (5) Soler-Illia, G.; Crepaldi, E. L.; Grosso, D.; Sanchez, C. *Curr. Opin. Colloid Interface Sci.* **2003**, *8*, 109–126.
- (6) Wan, Y.; Shi, Y. F.; Zhao, D. Y. *Chem. Commun.* **2007**, 897–926.
- (7) Melosh, N. A.; Lipic, P.; Bates, F. S.; Wudl, F.; Stucky, G. D.; Fredrickson, G. H.; Chmelka, B. F. *Macromolecules* **1999**, *32*, 4332–4342.
- (8) Brinker, C. J.; Lu, Y. F.; Sellinger, A.; Fan, H. Y. *Adv. Mater.* **1999**, *11*, 579.
- (9) Yang, P. D.; Zhao, D. Y.; Margolese, D. I.; Chmelka, B. F.; Stucky, G. D. *Nature* **1998**, *396*, 152–155.
- (10) Antonelli, D. M.; Ying, J. Y. *Angew. Chem., Int. Ed. Engl.* **1995**, *34*, 2014–2017.
- (11) Alberius, P. C. A.; Frindell, K. L.; Hayward, R. C.; Kramer, E. J.; Stucky, G. D.; Chmelka, B. F. *Chem. Mater.* **2002**, *14*, 3284–3294.
- (12) Brinker, C. J.; Lu, Y.; Sellinger, A.; Fan, H. *Adv. Mater.* **1999**, *11*, 579–585.
- (13) Nelson, J. *Science* **2001**, *293*, 1059–1060.
- (14) Coakley, K. M.; McGehee, M. D. *Chem. Mater.* **2004**, *16*, 4533–4542.
- (15) Halls, J. J. M.; Pichler, K.; Friend, R. H.; Moratti, S. C.; Holmes, A. B. *Appl. Phys. Lett.* **1996**, *68*, 3120–3122.
- (16) Savenije, T. J.; Warman, J. M.; Goossens, A. *Chem. Phys. Lett.* **1998**, *287*, 148–153.
- (17) Lunt, R. R.; Giebink, N. C.; Belak, A. A.; Benziger, J. B.; Forrest, S. R. *J. Appl. Phys.* **2009**, *105*, 053711.
- (18) Ravirajan, P.; Peiro, A. M.; Nazeeruddin, M. K.; Graetzel, M.; Bradley, D. D. C.; Durrant, J. R.; Nelson, J. *J. Phys. Chem. B* **2006**, *110*, 7635–7639.
- (19) Arias, A. C.; MacKenzie, J. D.; Stevenson, R.; Halls, J. J. M.; Inbasekaran, M.; Woo, E. P.; Richards, D.; Friend, R. H. *Macromolecules* **2001**, *34*, 6005–6013.
- (20) Masahiro, H.; Takumi, Y.; Mari, D.; Kouji, S.; Yoshio, M.; Masaaki, Y. *Appl. Phys. Lett.* **2006**, *88*, 213105.
- (21) Breeze, A. J.; Schlesinger, Z.; Carter, S. A.; Brock, P. J. *Phys. Rev. B* **2001**, *64*, 125205.
- (22) Ravirajan, P.; Haque, S. A.; Durrant, J. R.; Bradley, D. D. C.; Nelson, J. *Adv. Funct. Mater.* **2005**, *15*, 609–618.
- (23) van Hal, P. A.; Christiaans, M. P. T.; Wienk, M. M.; Kroon, J. M.; Janssen, R. A. J. *J. Phys. Chem. B* **1999**, *103*, 4352–4359.
- (24) Boucle, J.; Ravirajan, P.; Nelson, J. *J. Mater. Chem.* **2007**, *17*, 3141–3153.
- (25) van Hal, P. A.; Wienk, M. M.; Kroon, J. M.; Verhees, W. J. H.; Slooff, L. H.; van Gennip, W. J. H.; Jonkheijm, P.; Janssen, R. A. J. *Adv. Mater.* **2003**, *15*, 118–121.
- (26) Dovgolevsky, E.; Kirmayer, S.; Lakin, E.; Yang, Y.; Brinker, C. J.; Frey, G. L. *J. Mater. Chem.* **2008**, *18*, 423–436.
- (27) Kirmayer, S.; Dovgolevsky, E.; Kalina, M.; Lakin, E.; Cadars, S.; Epping, J. D.; Fernandez-Arteaga, A.; Rodriguez-Abreu, C.; Chmelka, B. F.; Frey, G. L. *Chem. Mater.* **2008**, *20*, 3745–3756.
- (28) Neyshadt, S.; Kalina, M.; Frey, G. L. *Adv. Mater.* **2008**, *20*, 2541–2546.
- (29) Kirmayer, S.; Neyshadt, S.; Keller, A.; Okopnik, D.; Frey, G. L. *Chem. Mater.* **2009**, *21*, 4387–4396.
- (30) Huynh, W. U.; Dittmer, J. J.; Libby, W. C.; Whiting, G. L.; Alivisatos, A. P. *Adv. Funct. Mater.* **2003**, *13*, 73–79.
- (31) Wenli, W.; HongBin, W.; CuiYing, Y.; Chan, L.; Yong, Z.; JunWu, C.; Yong, C. *Appl. Phys. Lett.* **2007**, *90*, 183512.
- (32) Wang, H.; Oey, C. C.; Djuricic, A. B.; Xie, M. H.; Leung, Y. H.; Man, K. K. Y.; Chan, W. K.; Pandey, A.; Nunzi, J. M.; Chui, P. C. *Appl. Phys. Lett.* **2005**, *87*, 023507.
- (33) Coakley, K. M.; McGehee, M. D. *Appl. Phys. Lett.* **2003**, *83*, 3380–3382.
- (34) Hwang, I.-W.; Cho, S.; Kim, J. Y.; Lee, K.; Coates, N. E.; Moses, D.; Heeger, A. J. *J. Appl. Phys.* **2008**, *104*, 033706–033714.
- (35) Tate, M. P.; Eggiman, B. W.; Kowalski, J. D.; Hillhouse, H. W. *Langmuir* **2005**, *21*, 10112–10118.
- (36) Crepaldi, E. L.; Soler-Illia, G. J. d. A. A.; Grosso, D.; Cagnol, F.; Ribot, F.; Sanchez, C. *J. Am. Chem. Soc.* **2003**, *125*, 9770–9786.
- (37) The weight percentages of the conjugated polymer in the films were calculated from the molar ratios in the precursor solution and assuming complete condensation of the titania precursor.
- (38) Erez, Y.; Huppert, D. *J. Phys. Chem. A* **2010**, *114*, 8075–8082.
- (39) Hediger, S.; Meier, B. H.; Kurur, N. D.; Bodenhause, G.; Ernst, R. R. *Chem. Phys. Lett.* **1994**, *223*, 283–288.
- (40) Liao, L. S.; Fung, M. K.; Cheng, L. F.; Lee, C. S.; Lee, S. T.; Inbasekaran, M.; Woo, E. P.; Wu, W. W. *Appl. Phys. Lett.* **2000**, *77*, 3191–3193.

- (41) Marion, D.; Wuthrich, K. *Biochem. Biophys. Res. Commun.* **1983**, *113*, 967–974.
- (42) Elena, B.; de Paepe, G.; Emsley, L. *Chem. Phys. Lett.* **2004**, *398*, 532–538.
- (43) Hayashi, S.; Hayamizu, K. *Bull. Chem. Soc. Jpn.* **1991**, *64*, 685–687.
- (44) Nguyen, T.-Q.; Wu, J.; Doan, V.; Schwartz, B. J.; Tolbert, S. H. *Science* **2000**, *288*, 652–656.
- (45) Nguyen, T.-Q.; Wu, J.; Tolbert, S. H.; Schwartz, B. J. *Adv. Mater.* **2001**, *13*, 609–611.
- (46) Posudievsky, O. Y.; Telbiz, G. M.; Rossokhaty, V. K. *J. Mater. Chem.* **2006**, *16*, 2485–2489.
- (47) Ayzner, A. L.; Tassone, C. J.; Tolbert, S. H.; Schwartz, B. J. *J. Phys. Chem. C* **2009**, *113*, 20050–20060.
- (48) Wei, T.-C.; Hillhouse, H. W. *Langmuir* **2007**, *23*, 5689–5699.
- (49) Neyshadt, S.; Frey, G. L. *Microporous Mesoporous Mater.* **2011**, *142*, 708–715.
- (50) Eggiman, B. W.; Tate, M. P.; Hillhouse, H. W. *Chem. Mater.* **2006**, *18*, 723–730.
- (51) Choi, S. Y.; Lee, B.; Carew, D. B.; Mamak, M.; Peiris, F. C.; Speakman, S.; Chopra, N.; Ozin, G. A. *Adv. Funct. Mater.* **2006**, *16*, 1731–1738.
- (52) Falcato, P.; Grosso, D.; Amenitsch, H.; Innocenzi, P. *J. Phys. Chem. B* **2004**, *108*, 10942–10948.
- (53) Although films prepared with F127 and P123 surfactants have different packing of spherical aggregates, that difference alone can not account for the similarity of the lattice parameters calculated for the two structures.
- (54) Boettcher, S. W.; Bartl, M. H.; Hu, J. G.; Stucky, G. D. *J. Am. Chem. Soc.* **2005**, *127*, 9721–9730.
- (55) Adams, D. M.; et al. *J. Phys. Chem. B* **2003**, *107*, 6668–6697.
- (56) Chang, T. W. F.; Musikhin, S.; Bakueva, L.; Levina, L.; Hines, M. A.; Cyr, P. W.; Sargent, E. H. *Appl. Phys. Lett.* **2004**, *84*, 4295–4297.
- (57) Vooren, A. V.; Lemaire, V.; Ye, A.; Beljonne, D.; Cornil, J. *ChemPhysChem* **2007**, *8*, 1240–1249.
- (58) Beek, W. J. E.; Janssen, R. A. J. *J. Mater. Chem.* **2004**, *14*, 2795–2800.
- (59) Asbury, J. B.; Hao, E.; Wang, Y.; Lian, T. *J. Phys. Chem. B* **2000**, *104*, 11957–11964.
- (60) Schmidt-Rohr, K.; Spiess, H. W. *Multidimensional Solid-State NMR and Polymers*; 1st ed.; Academic Press: San Diego, 1994.
- (61) Crocker, M.; Herold, R. H. M.; Wilson, A. E.; Mackay, M.; Emeis, C. A.; Hoogendoorn, A. M. *J. Chem. Soc., Faraday Trans.* **1996**, *92*, 2791–2798.
- (62) Shenderovich, I. G. *Russ. J. Gen. Chem.* **2006**, *76*, 501–506.
- (63) Steinbeck, C. A.; Hedin, N.; Chmelka, B. F. *Langmuir* **2004**, *20*, 10399–10412.
- (64) Stilbs, P. *J. Colloid Interface Sci.* **1983**, *94*, 463–469.
- (65) Brown, S. P.; Spiess, H. W. *Chem. Rev.* **2001**, *101*, 4125–4155.
- (66) Chen, Q.; Jia, Y. Y.; Liu, S. B.; Mogilevsky, G.; Kleinhammes, A.; Wu, Y. *J. Phys. Chem. C* **2008**, *112*, 17331–17335.
- (67) The significantly higher  $^1\text{H}$  intensity at ca. 6.7 ppm is attributed to the presence of more nondeuterated moisture accompanying the longer hydrophilic PEO blocks in F127, c. t.
- (68) Schwartz, B. J. *Annu. Rev. Phys. Chem.* **2003**, *54*, 141–172.
- (69) Goh, C.; Scully, S. R.; McGehee, M. D. *J. Appl. Phys.* **2007**, *101*, 114503.
- (70) Brabec, C.; Dyakonov, V.; Parisi, J.; Sariciftci, N. S. *Organic Photovoltaics: Concepts and Realization*; Springer: Heidelberg, 2003.
- (71) Barry, P. R.; Diana, P. B.; Stephen, R. F. *Phys. Rev. B: Condens. Matter Mater. Phys.* **2007**, *75*, 115327.
- (72) Wei, Q.; Hirota, K.; Tajima, K.; Hashimoto, K. *Chem. Mater.* **2006**, *18*, 5080–5087.
- (73) Fan, Q.; McQuillin, B.; Bradley, D. D. C.; Whitelegg, S.; Seddon, A. B. *Chem. Phys. Lett.* **2001**, *347*, 325–330.